Dual Comb Spectrometry of Solid Samples

Mémoire

Joseph Skehan

Maîtrise en physique - avec mémoire
Maître ès sciences (M. Sc.)

Québec, Canada

Dual Comb Spectrometry of Solid Samples

Mémoire

J Connor Skehan

Sous la direction de:

Claudine Allen, directrice de recherche
Jérôme Genest, codirecteur de recherche

Résumé

L'objectif de ce mémoire est de partager les connaissances obtenues lors de mon travail sur la spectroscopie à deux peignes et ses applications sur les matériaux solides.

Pour y parvenir, certain sujets connexes sont élaborés. Dans l'ordre, on y aborde la physique des lasers, le verrouillage et la stabilisation des modes, l'interférométrie générale et celle des peignes, ainsi que la modification des impulsions des peignes de fréquence en utilisant l'ptique non-linéaires.

On présente ensuite deux études expérimentales. La première porte sur la combinaison de la spectroscopie à deux peignes avec la technique pompe-sonde et la seconde sur l'analyse de la variance *baseline* en contexte de la spectroscopie à deux peignes.

Abstract

The goal of this memoire is to communicate my work regarding the application of dual comb spectroscopy to materials beyond traditional gas phase spectroscopy.

A variety of topics required to understand my work are presented, such as general laser physics, mode-locking, stabilization of the repetition rate and carrier envelope offset, interferometry, dual comb spectroscopy, and the modification of said combs via non-linear optics.

Two experimental studies are presented as well. These include the combination of dual comb spectroscopy with the pump-probe technique, as well as an analysis of baseline variance in context of dual comb spectroscopy.

Table des matières

Liste des figures

Dedicated, like all important things, to my friends and family.

On the planet Earth, man had always assumed that he was more intelligent than dolphins because he had achieved so much - the wheel, New York, wars and so on - whilst all the dolphins had ever done was muck about in the water having a good time. But conversely, the dolphins had always believed that they were far more intelligent than man - for precisely the same reason.

Douglas Adams, Hitchhikers Guide to the Galaxy

Remerciements

The completion of my master's degree in physics has been a lifelong pursuit, and its success stems primarily from the support of my parents and Uncle in my childhood. Their eternal encouragement, support, and understanding are some of the greatest gifts I have ever been granted. Being taught to seek answers when I had questions, to take pleasure in exploration, and to approach life with an open mind are just some of the things for which I owe them thanks.

Secondly, I would like to thank Dr. Claudine Allen, Dr. Jérôme Genest, and Dr. Ian Coddington for their friendship, their faith in my abilities, and the knowledge they passed on. In particular, Dr. Allen bridged the gap between materials science and optics, Dr. Genest introduced me to signal processing, advanced electronics, and frequency combs, and Dr. Coddington deepened by understanding of both frequency combs and non-linear optics.

Next, I would like to thank my colleagues. In particular, Dan Herman, Nicolas Bourbeau-Hébert, and Vincent Michaud-Belleau. Their patience and willingness to take time out of their own research to help me is admirable. The latter two, as well Dr. Allen, and Dr. Genest being especially helpful in my understanding of the French language.

Finally, I would like to thank FRQNT for financial support. In particular, my thanks goes to Dr. Jérôme Genest whose research funds paved the way for my education in Québec, and who arranged my collaboration with Dr. Coddington at NIST, and to Dr. Coddington whose research funds supported my education as well.

Introduction

This memoire focuses on the fabrication, stabilization, and application of frequency combs, particularly their use in dual comb spectroscopy (DCS), a technique which allows for the rapid, ultra-precise detection of optical signals. Traditionally, the technique has been used in gas phase absorption spectroscopy for its extreme precision, but my work focuses on its applications to the reflective and absorptive properties of solid-state materials.

Fully stabilized, mode-locked lasers, also called frequency combs, are represented in the frequency domain by a series of equally spaced, delta-like lines "teeth", which correspond to optical modes, and are modulated by some envelope function. In the time domain, these combs often manifest as wave packets, or pulses.

The frequency of these teeth have two degrees of freedom, and can thus be fully described by two parameters. The first of these parameters is the repetition rate of the pulsed source, f_{rep}, which determines mode spacing in the frequency domain, and the second is the phase relationship between successive periods, called the "carrier envelope offset", or CEO. This CEO is commonly expressed as a frequency offset from zero, f_{CEO}, common to all modes in the spectral domain.

Mixing the fields of two such lasers, differing in f_{rep} by Δf_{rep}, on a photodetector produces a time-varying interference pattern called an "interferogram" (IGM). This signal may be subsequently Fourier transformed, allowing for the retrieval of spectral domain information.

Chapter 1 presents a review of the physics underpinning dual comb spectroscopy and the research done in this memoire. It begins with fundamental laser physics, and shows how to create a mode-locked laser. Next, a variety of mathematical concepts are presented (Fourier transformations, dispersion relations, and Kramers-Kronig relations), along with an explanation of how to actually stabilize a mode-locked laser, and why the method works. Next, various types of frequency combs are presented, along with an overview of interferometry and dual comb spectroscopy in particular. Finally, the topic of non-linear optics is briefly discussed, as it has a large impact on my work.

Chapter 2 and chapter 3 present data and analysis covering my work at Université Laval (ULaval) and at the National Institute of Standards and Technology (NIST).

My work done at ULaval focuses on combining dual comb spectroscopy with the well known pump-probe technique, thereby allowing for the spectral study of material excitation and relaxation rates. Chapter 2 begins by defining pump probe spectroscopy and showing what frequency combs add to the technique. Next, previous experiments are repeated to demonstrate mastery of the system and give credibility to future results. Finally, dual comb spectroscopy is combined with the pump probe technique, and preliminary results are presented.

My work done at NIST focuses on understanding the various effects which can change the spectral baseline of a measurement in the context of dual comb spectroscopy. Chapter 3 begins by defining what a baseline is, and by defining various referencing techniques. Next, a mathematical model is developed which provides insight into the assumptions of each of the different referencing techniques. Then, various methods to induce and or suppress baseline variance are tested. Finally, a flat spectral baseline over the period of four hours is demonstrated using one of the techniques described previously.

Lastly, a brief conclusion is presented.

Chapitre 1

Theory

This first chapter focuses on the physics required to understand later chapters. It starts with basic laser physics, and works its way up to the creation of a frequency comb, dual comb spectroscopy, and the field of non-linear optics.

Specifically, it begins by covering laser basics, and how to mode-lock a laser. We discuss spontaneous emission, three state systems, optical feedback, and cavity modes. We also discuss pulse formation via modal interference, and how to produce pulses using saturable absorbing mirrors, non-linear polarization rotation, and non-linear optical loop mirrors.

A short section of math follows, along with the specifics of mode-locked laser stabilization and the presentation of various other types of combs. The Fourier transform limitations of pulsed lasers are discussed, along with the basics of dispersion and the Kramers-Kronig relations. It is then shown how to stabilize the repetition rate and carrier envelope offset of a mode-locked laser, and how, in doing so, a frequency comb is created. Other types of combs are reviewed as well, including micro-resonator and electro-optical combs.

Next, interferometry and dual comb spectroscopy in particular are discussed. Both the single beam and multi-beam cases of interferometry are discussed, using Michelson and Fabry-Perot interferometers as examples. Using this basis in interferometry, DCS is described, starting with the formation of heterodyne beats and a radio frequency comb. The symmetric and asymmetric cases of DCS are explained, and the impact of unintentional multi-path interference is discussed.

Finally, the field of non-linear optics is presented. Specifically, we look at χ^2 processes, focusing on second harmonic generation, as well as χ^3 processes, focusing on the Kerr non-linearity.

1.1 Laser Basics

In general, a laser (light amplification by stimulated emission of radiation), [1] exploits the discrete energy levels in some quantum system, hereafter referred to as the gain medium, to amplify light via stimulated emission, the process by which one photon interacts with some electron in an excited state, forcing it to radiatively relax to a lower state. Here, the difference in energy between the electron's excited and relaxed states must be equal to the incoming photon's energy.

The emitted photon is of the same frequency, phase, direction, and optical polarization of the stimulating photon, giving rise to a property known as coherence. For a light source to be coherent with some other light source means that there exists some fixed phase relationship in either space or time between the two sources. Stimulated emission of radiation is just one of many ways to produce a coherent source.

For certain gain media, including erbium doped glass (see figure 1.1), the gain medium used primarily throughout this memoire, the energy levels in question are not of single frequency, but instead exist over a broad bandwidth. This is primarily due to the splitting and shifting of energy levels, as caused by some external electric field (in this case, the neighboring atoms). This process of splitting and shifting is referred to as the Stark effect. Here, not only are the absorption and emission spectra broadened, but the the emission spectrum is red-shifted from its absorption spectrum by the same process [2].

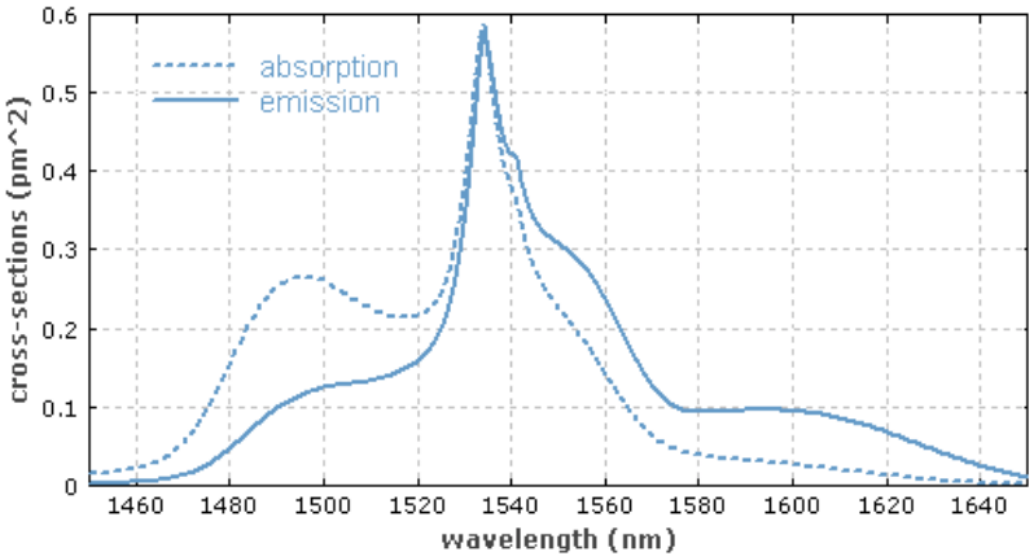

FIGURE 1.1 – The absorption and emission profiles of Erbium 3+ ions in phosphate (P_2O_5) glass. Note that the spectra, being influenced heavily by the local electric field, will differ between various types of glasses. Credit RP Photonics & Honaken's work in 1997 [3].

For erbium lasers, the basic mechanism of action is as follows (see figure 1.2) : 980 nm light

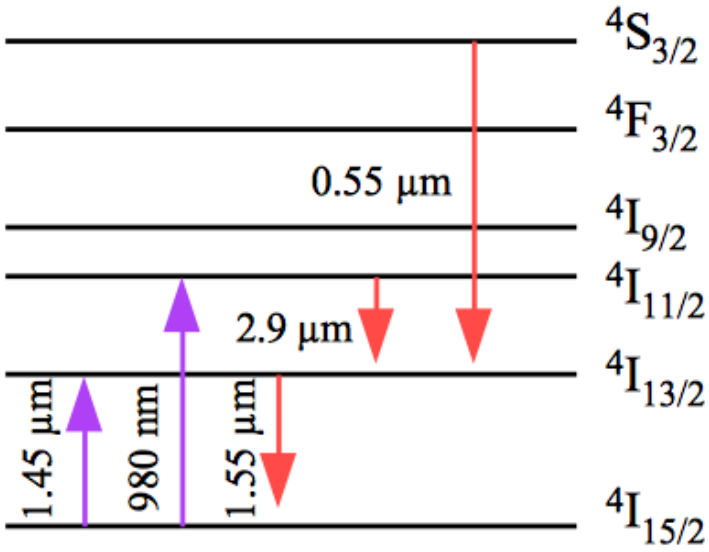

FIGURE 1.2 – Excitation and relaxation of energy levels in Erbium 3+ ions, as denoted by their Stark manifolds (solid lines). These manifolds consist of many energy levels split from a central point due to the Stark effect, labeled by their "term symbols", a shorthand used to describe the total angular momentum quantum numbers in a multi-electron atom. The wavelength value provided for each transition uses the center wavelength of each Stark manifold [4].

is absorbed by a ground-state (labeled $^4I_{15/2}$ in figure 1.2) erbium atom, pushing an electron into an unstable, short lived, high-energy state ($^4I_{11/2}$). This electron then quickly decays to a metastable state ($^4I_{13/2}$).

The short electron life time in the upper-most level allows for the rapid pumping of electrons to the metastable state, while the longer lifetime of the metastable level enables electrons to accumulate in that state. There can therefore exist more electrons in the metastable level than in the ground state. This situation is called population inversion, and is necessary for optical amplification.

This is because, in a system experiencing population inversion, more electrons are in a state from which stimulated emission occurs than there are electrons in a state from which absorption occurs. Any incoming light is thus more likely to induce stimulated emission than it is to be absorbed, and optical amplification can occur.

To obtain a laser, one needs to recycle part of the amplified optical field such as to continuously sustain the coherent emission process. This optical feedback is typically achieved by placing the gain medium inside a cavity made of partially reflective mirrors, as shown in figure 1.3. In the special case presented in the figure, one mirror is perfectly reflective at the laser wavelength while still allowing the pump to couple in the cavity. The second mirror is partially reflective

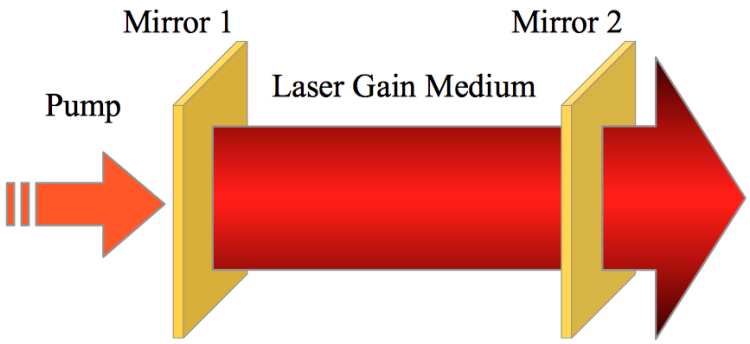

FIGURE 1.3 – A Laser cavity. Here, a gain medium resides between two mirrors. Mirror 1 is fully reflective, while mirror 2 is partially reflective and partially transmissive. The mechanism of pumping here is general, but could be electrical, optical, etc.

and allows a fraction of the field in the cavity to escape as the laser output.

An important result stemming from the fact that a laser field is generated inside a cavity, is the fact that only specific modes of oscillation are allowed within said cavity. In essence, standing waves inside the cavity, or modes, interfere constructively, while any fields of offset frequency interfere deconstructively. The practical result being that the output of such a laser consists of discrete modes corresponding to frequencies which are resonant with the cavity.

Many modes can exist within the cavity, each with a wavelength corresponding, in a simplistic picture which is sufficient for the moment, to a different integer multiple of the cavity's optical length, as seen in equation 1.1. The separation between any of two of these modes inside the cavity, then, is determined by the cavity's optical round trip length, as seen in equation 1.2.

$$L = m \cdot \lambda \tag{1.1}$$

$$\Delta v = \frac{c}{L} \tag{1.2}$$

Where L is the cavity's round trip optical length, m is the mode number, λ is the wavelength of light inside the cavity, Δv is the separation (in frequency space) between the m^{th} and $m+1^{th}$ modes, and c is the speed of light,. It should be noted here that this model assumes a dispersion free cavity. Later discussions will not include this assumption.

In practice, laser cavities are typically much longer than the wavelengths of light traveling inside them, and thus values of m are high, resulting in a small frequency difference between subsequent modes. For example, for a 1.0 m long (physical length) linear cavity made of a medium whose index of refraction, n, is 1.5, (L = 3 m), m = $1e^6$ at 1500 nm, and m = $9.68e^5$ at 1550 nm, with 32,000 modes between the given wavelengths.

1.2 Mode-Locked Lasers

A mode-locked laser usually produces a series of short wave packets (on the order of pico or femtoseconds), separated from each other both in space and in time by some regular quantity related to the round trip distance and time required to traverse the cavity. As described above in section 1.1, laser cavities only support specific standing waves, or longitudinal modes.

The action of mode-locking, at the most basic approach, is to force a fixed phase relationship between these longitudinal cavity modes. Looking at the cavity's output, as shown in figure 1.4, the fixed phase relation creates a repeating interference pattern between modes. At regular time intervals, equal to $\frac{1}{f_{rep}}$, all modes are "in phase" and interfere constructively to produce pulses.

Between these brief moments of constructive interference, modes interfere in a mostly destructive manner. In practice, the large number of modes sustained by the gain medium and cavity produce a near zero field between the pulses. Inside the cavity, this corresponds to, when the mode-locking condition is met, a single pulse circulating in the cavity.

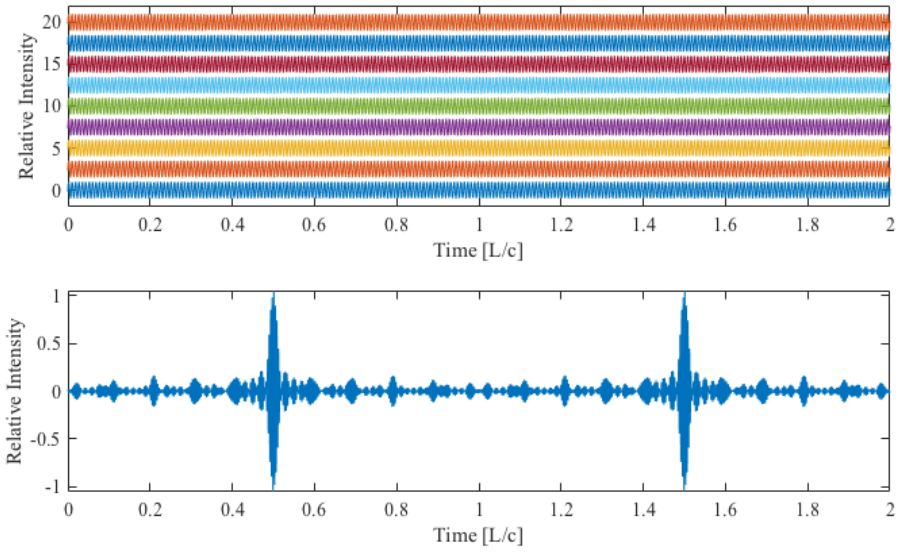

FIGURE 1.4 – Cavity modes with a fixed phase relationship (above), with an applied vertical offset for ease of viewing, and their summation (below) to produce a pulse which travels the length of the cavity. Here, only a few modes (50 used in the simulation, 9 pictured) are used in the calculation. Data is presented in the time domain, in units of $\frac{L}{c} = \frac{1}{f_{rep}}$

The creation of a fixed phase relationship between cavity modes can be implemented in a variety of ways. One common method is the application of saturable absorbing mirrors (SAMs) [6]. SAMs are typically constructed via the coating of some mirror, generally dielectric, with a semiconducting media which exhibits saturable absorption (SA).

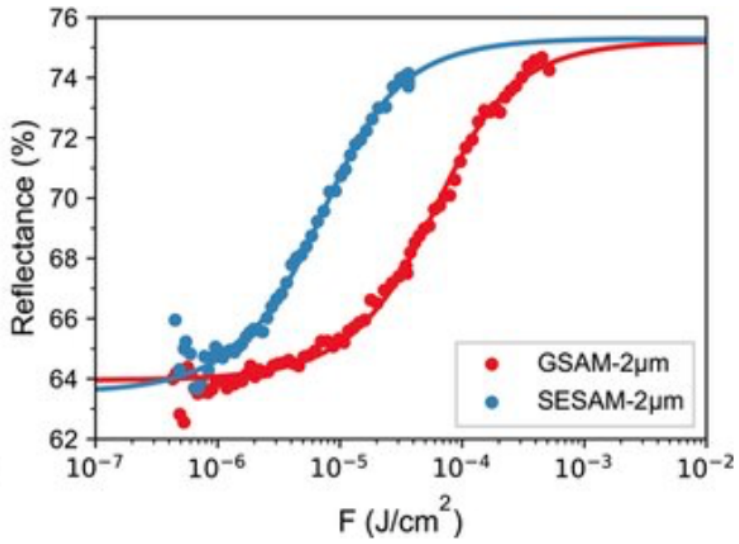

FIGURE 1.5 – Reflectivity response of a semiconducting saturable absorbing mirror (SESAM) and a graphene saturable absorbing mirror (GSAM) after excitation by various fluences of light. Credit Wang & Blau, 2017 [5]. Here, F stands for the fluence, in units of Joules per cm^2.

The primary mechanism of action for SAMs is to favor high peak power in the cavity by selectively absorbing low intensity light. Due to the mirror's SA properties, the mirror's reflectively depends partially on the fluence (energy per unit area) of the incident light. For low intensity light, the mirror's reflectively, R, is relatively constant with respect to fluence, but for high intensity light, $R = R_0 + \Delta R$, where R_0 is the linear reflectivity, and ΔR is a positive value called the modulation depth. Figure 1.5 shows the non-linear response of two SAMs to increasing fluence, F. After some time, the SAM will relax back to its initial state.

An interesting effect of the mode-locking mechanism of SAMs is that pulses may be formed via their use which are much shorter than their relaxation rate. This is because the only requirements placed on the time-domain response of a SAM are that a) its absorption saturates quickly enough to force a phase relationship between cavity modes, and b) the SAM relaxes to its unsaturated state before the pulse returns to interact with the saturable absorber.

Another common mode-locking mechanism, and the one used in the Menlo combs at Université Laval, can be created via the use of non-linear polarization rotation (NPR) in optical fiber [7]. Here, a non-linear change in the optical field's polarization state is created when high intensity light passes though a fiber which is not polarization maintaining. If the output of the fiber then passes through a polarizing filter which is tuned to selectively allow transmission of the new optical polarization state, the final output is now intensity dependent. Light which does not contribute to pulse formation will not undergo the polarization shift, and is thus absorbed by the filter. On the other hand, light which does contribute to pulse formation will pass. This again favors pulse formation in the cavity and hence forces a fixed phase relation-

ship. Alternatively, the same method may be applied using a highly birefringent (polarization maintaining) fiber and Faraday rotators [8; 9].

A third commonly used mechanism for the mode-locking of lasers is the non-linear optical loop mirror (NOLM) [10]. Here, the "mirror" is formed by connecting together the two output ports of a 2x2 fiber coupler, creating a loop. Light coming from an input port will couple into the loop and propagate along two distinct paths, one clockwise around the loop and the other anti-clockwise. When these waves meet again at the coupler after traversing the loop, the waves interfere, and this interference determines what amount of power is sent back into which input port. In the linear regime, the two paths around the loop have the same optical length, and thus return to the coupler in phase. Assuming a $50:50$ coupling ratio between output ports, a lossless loop, and no change in optical polarization state during propagation, this creates a perfect, 100% reflective mirror. All light which enters from input port A will return to input port A.

In the regime of high intensity light (the non-linear regime), the light itself will modify the refractive index of the medium, as a function of that light's intensity. This means that some low intensity light traversing the loop will see a different optical path length than would some high intensity light. Indeed, when in the non-linear regime, and when the coupling ratio is anything other than $50:50$, light traveling around the loop clockwise does see a different path than light which travels anti-clockwise around the loop. When the two finish their round trip and return to the coupler, their instantaneous phases will be different. This in turn changes the interference between them, and therefore the amount of power sent back into each input port. The reflectivity of the NOLM must therefore be a function of intensity. By modifying various parameters of the system, such as the input power, coupling ratio, loop length / material, etc, an artificial saturable absorbing mirror may be created and used to mode-lock a laser.

Both NPR and NOLMs rely on a non-linear relation between the optical field, E, and the material polarization, P, which changes the index of refraction via the Kerr effect. This relation occurs quickly enough that it is often treated as being instantaneous [11]. These kinds of non-linear effects will be discussed in further detail in section 1.8. Such mode-locking schemes over several advantages over the use of SAMs, namely the fact that the system can respond nearly instantaneously to losses or changes within the resonator, and that the pulse is treated symmetrically about its center in time, as opposed to a SESAM, which treats the leading edge of the pulse differently than the trailing edge. In general, these effects lead to a mode-locking scheme which tends towards lower noise.

Mode-locked laser formation places a variety of requirements on the physical components of the system. Not only is some method of forcing a fixed phase relationship required, but so is a broad bandwidth gain medium. This is because pulse formation requires constructive interference between many cavity modes, and thus a gain medium broad enough to support

the many modes is required. Erbium 3+ ions in glass fill this role well, given that their gain bandwidth covers tens of THz [12].

1.3 Transform-Limited pulses, Dispersion, and Kramers-Kronig Relations

The Fourier transform (FT) and its inverse (IFT) prescribe a unique bi-directional relation between a signal in the time or space domains and the constituent frequencies which may be used to express the same signal in the frequency domain. This relationship is defined in equations 1.3 and 1.4, where the Fourier transform is applied to some time varying function, $x(t)$, to yield its equivalent in the frequency domain, $X(\omega)$, where both $x(t)$ and $X(\omega)$ are generally allowed to be complex functions.

$$X(\omega) \;=\; \int_{-\infty}^{\infty} x(t)e^{-i\omega t}dt \tag{1.3}$$

$$x(t) \;=\; \frac{1}{2\pi}\int_{-\infty}^{\infty} X(\omega)e^{-i\omega t}d\omega \tag{1.4}$$

For a pulsed signal having a given spectral amplitude, there exists a narrowest possible temporal shape. As this relation is defined by the Fourier transform, a temporal pulse respecting this condition is sometimes called "transform limited". This is the result of the uncertainty principle [13]. Any two physical quantities forming a Fourier pair are bound by this limitation (i.e. localization of one implies delocalization of the other).

The time-bandwidth product (TBWP) of a pulsed signal is a unitless quantity defined as the product between the duration of the signal in the time domain (Δt) and its width in the spectral domain ($\Delta f = \frac{\Delta\omega}{2\pi}$), and can be used to quantify how close a signal is to it's transform limit. The transform limited TBWP depends upon the spectral shape of the signal. For instance, using the amplitude spectrum's full-width half-max (FWHM), the transform limited TBWP is $\sim$0.315 for sech^2 pulses and $\sim$0.44 for Gaussian pulses [14; 15; 1]. For reference, the uncertainty principle relation fixes an absolute minimum of 0.25 for the TBWP.

On the other hand, when given *both* the spectral amplitude *and* phase profile of the pulse, there exists only one possible solution to the Fourier transform. It so happens that the phase spectrum required for a transform limited pulse is one which is frequency independent. All pulses which are not transform-limited, then, must have a phase which depends on frequency. These pulses are referred to as being chirped.

In some media, different frequencies of light can acquire different phase shifts while traveling through a medium. We call these dispersive media, and they have a special importance when modeling the propagation of pulses, as they effect the pulse shape in the time domain.

A pulse traveling through such a media can be described using equation 1.5.

$$E(x,t) \;=\; \int_{-\infty}^{\infty} \tilde{E_0}(\omega) e^{i\beta(\omega)x}\; e^{-i\omega t} d\omega \tag{1.5}$$

Here, we assume that the field can be described by the plane wave solution to the wave equation. $\tilde{E_0}(\omega)$ is a complex phasor which describes the spectral amplitude and phase at some initial position in space and time (x=0, t=0), and β is the propagation constant, which we can think of as the phase shift $\Delta\phi$ acquired for some frequency of light ω, per distance L through the medium, as expressed by equation 1.6.

$$\beta(\omega) \;=\; \frac{\Delta\phi(\omega)}{L} \tag{1.6}$$

In equations 1.5 and 1.6, we see that β is written as a function of ω. In fact, in dispersive materials where the propagation constant depends on the frequency, it is often convenient to express $\beta(\omega)$ as a Taylor expansion about its center or mid-band frequency, ω_0, as seen in equation 1.7.

$$\beta(\omega) \;=\; \beta_0 \;+\; \beta_0' \cdot (\omega \;-\; \omega_0) \;+\; \beta_0'' \cdot \frac{(\omega \;-\; \omega_0)^2}{2} \tag{1.7}$$

Here, $\beta_0 = \beta(\omega_0)$, $\beta_0' = \beta'(\omega_0)$, and $\beta_0'' = \beta''(\omega_0)$, β' is the first derivative of β with respect to ω, β'' is the second derivative of β with respect to ω, and we assume that the field is narrow around ω_0.

Three definitions are important here. Firstly, phase velocity, v_ϕ, represents the speed at which the carrier phase under the envelope propagates through the medium. Secondly, the group velocity, v_g, describes the speed at which the group, or pulse, travels through the medium. And finally, the group velocity dispersion, GVD, of the system describes the rate of change of the inverse group velocity with respect to ω.

For a monochromatic field at ω_0, 2π of phase is accumulated for each length in space $\frac{2\pi}{\beta_0}$, and the same is accumulated for each length in time $\frac{2\pi}{\omega_0}$. We can therefore conclude that a point of constant phase must travel at $v_\phi(\omega_0) = \frac{distance}{time} = \frac{\omega_0}{\beta_0}$. This of course implies that $\beta_0 = \frac{\omega_0}{v_\phi(\omega_0)}$.

A pulse, however, is not a monochromatic source. To better understand pulse propagation, we therefore need to analyze how β changes with respect to ω. To see how this works, let's rewrite equation 1.5 using the first two terms of the Taylor expansion of ω about β (i.e., we write $\omega(\beta) = \omega_0 + \omega_0'(\beta - \beta_0)$), keeping in mind that ω is implicitly a function of β, and using the same labeling scheme as was used for the Taylor expansion of β previously. This new expression is shown in equation 1.8.

$$
\begin{aligned}
E(x,t) &= \int_{-\infty}^{\infty} d\omega\ \tilde{E}_0(\omega)\ e^{i\beta(\omega)x} e^{-i\omega t} \\
&= \int_{-\infty}^{\infty} d\omega\ \tilde{E}_0(\omega)\ e^{i\beta x} e^{-i[\omega_0 + \omega_0'(\beta-\beta_0)]t} \\
&= \int_{-\infty}^{\infty} d\omega\ \tilde{E}_0(\omega)\ e^{i\beta x} e^{-i\omega_0 t} e^{-i\omega_0'\beta t} e^{i\omega_0'\beta_0 t} \\
&= \int_{-\infty}^{\infty} d\omega\ \tilde{E}_0(\omega)\ e^{i\beta x} e^{-i\omega_0 t} e^{-i\omega_0'\beta t} e^{i\omega_0'\beta_0 t} e^{i\beta_0 x} e^{-i\beta_0 x} \\
&= e^{i(\beta_0 x - \omega_0 t)} \int_{-\infty}^{\infty} d\omega\ \tilde{E}_0(\omega)\ e^{i(\beta-\beta_0)\cdot(x-\omega_0' t)}
\end{aligned}
\tag{1.8}
$$

We see two terms in the final expression of this equation. The one which is outside the integral represents a single, monochromatic frequency which has a phase velocity $v_\phi = \frac{\omega_0}{\beta_0}$, as expected. The term inside the integral, however, represents an envelope or wave packet which travels at a velocity $v_g = \omega_0' = \frac{d\omega}{d\beta}|_{\omega_0}$ (from the Taylor expansion of ω about β). This in turn implies that $\frac{1}{v_g(\omega_0)} = \frac{d\beta}{d\omega}|_{\omega_0} = \beta_0'$.

A nearly identical argument may be used to show that $\beta_0'' = \frac{d}{d\omega}(\frac{1}{v_g(\omega_0)}) = \text{GVD}$. Alternatively, we can simply remember that GVD represents the change in group velocity with respect to frequency. From this, we can conclude that for a β''=0 material, the pulse shape remains temporally unchanged during propagation, since all frequencies have the same group velocity. For non-zero GVD materials, however, because the group velocity is different for different frequencies of light, a transform limited pulse will stretch in time, becoming chirped. For an alimited pulse, it is subject to broadening or compression depending on initial chirp and on the sign of β''. Such behavior is used to compress pulses to their Fourier limit, thereby producing the highest peak power available for the given signal. See figure 1.6 for a visual representation of the chirp a transform limited pulse will acquire having traveled through a $\beta \neq 0$ material.

Finally, an important relationship between the phase and intensity of light in the frequency domain, after passing through some absorptive media, is provided by the Kramers-Kronig relation (derived in its entirety in A.1). For now, let's assume that some light is sent into an optical system, is somehow changed by that system, and that some amount of light then leaves the system. This can be expressed mathematically below in equation 1.9.

$$
E_{out}(\omega) = E_{in}(\omega) H(\omega) \tag{1.9}
$$

In such an expression, $H(\omega)$ is called the transfer function, is allowed to be complex such that $H(\omega) = H_1 + iH_2$, and describes the action of the material on the input field to produce the output. It has an associated impulse response, $h(t)$, which is real.

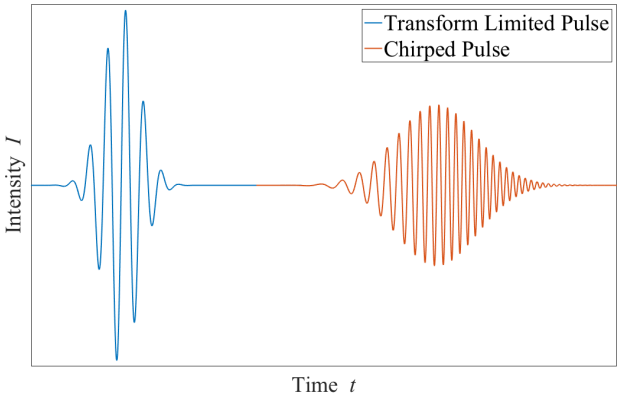

FIGURE 1.6 – A wave packet moving in space at some velocity v_g. After experiencing GVD, the pulse is stretched, since its constituent frequencies have different group velocities. In the picture above, higher frequencies travel with higher group velocity (and are therefore temporally ahead) of their lower frequency counter parts. We therefore know that β" is positive in the medium through which the transform limited pulse travels. In doing so, the peak power is reduced considerably.

A variety of derivations are found in the literature, but they all follow the same basic premise [16]. The condition of causality forces the impulse response of such a system to be 0 for $t < 0$. We can therefore think of the impulse response function as being some arbitrary real function multiplied by a step function centered at the origin. This in turn, imposes a relationship between the real and imaginary parts of the transfer function [17]. This relationship is seen in equations 1.10 and 1.11.

$$H_1(\omega) = \frac{1}{\pi} PV \int_{-\infty}^{\infty} \frac{H_2(\omega')}{\omega - \omega'} d\omega' \tag{1.10}$$

$$H_2(\omega) = -\frac{1}{\pi} PV \int_{-\infty}^{\infty} \frac{H_1(\omega')}{\omega - \omega'} d\omega' \tag{1.11}$$

Where PV refers to the Cauchy principle value (found by replacing the limits of the integral with some variable, ξ, and taking the limit of the integral as ξ approaches $\pm\infty$).

A more interesting physical result in the field of material optics arises when the transfer function in question is the electric susceptibility, χ, which is used to describe the polarization response, $P(\omega)$ of a material to an incident electric field $E(\omega)$, as seen in 1.12 where ϵ_0 is the electric permittivity.

$$P(\omega) = \epsilon_0 \chi(\omega) E(\omega) \tag{1.12}$$

Here, we note that $\chi = \chi_1 + i\chi_2$ serves the same role as $H(\omega)$ from before, it can thus be expressed in the same way. When we assume a linear relationship between $P(\omega)$ and $E(\omega)$, and know that $\chi_1(\omega) = \chi_1(-\omega)$ and $\chi_2(\omega) = -\chi_2(-\omega)$ for all real values of ω, we are able to write the Kramers-Kronig relation as follows in equations 1.13 and 1.14 [17].

$$\chi_1(\omega') = \frac{2}{\pi} PV \int_0^\infty \frac{\omega \chi_2(\omega)}{\omega^2 - \omega'^2} d\omega \tag{1.13}$$

$$\chi_2(\omega') = -\frac{2\omega'}{\pi} PV \int_0^\infty \frac{\chi_1(\omega) - 1}{\omega^2 - \omega'^2} d\omega \tag{1.14}$$

Keeping in mind that $\chi = \hat{n}^2 - 1$, we might desire a relationship between the real and complex parts of the refractive index, $\hat{n}(\omega) = n(\omega) + i\kappa$, where $n(\omega) = \frac{c}{v}$ and κ is the attenuation coefficient. Unfortunately, $\hat{n}(\omega)$ is not actually a response function itself but is instead an analytic function of the system's response function [18].

We are thus unable to directly use the Kramers-Kronig relations to relate $n(\omega)$ to κ. That being said, so long as the system is minimum phase, you can still uniquely find $n(\omega)$ from κ and vice versa.

The relationship between the real and imaginary parts of the complex refractive index, $\hat{n}(\omega)$, is defined by the equations below (equations 1.15 & 1.16) [16].

$$n(\omega') = 1 + \frac{2}{\pi} PV \int_0^\infty \frac{\omega \kappa(\omega)}{\omega^2 - \omega'^2} d\omega \tag{1.15}$$

$$\kappa(\omega') = -\frac{2\omega'}{\pi} PV \int_0^\infty \frac{n(\omega) - 1}{\omega^2 - \omega'^2} d\omega \tag{1.16}$$

In general, these relations tell us that in a minimal phase system, any absorption of light in a medium must come with a change in index of refraction (and thus phase), and that any change in phase or index of refraction must come hand in hand with a change in absorbance.

1.4 Mode-Locked Laser Stabilization - the Creation of a Frequency Comb

In general, a frequency comb is a laser source in which the frequency domain spectra is made of a series of well known, stable, and equally spaced, delta-like peaks called teeth. Fully stabilized, mode-locked lasers are a natural fit and were the first sources used as optical frequency combs.

Two parameters are of key importance when discussing a mode-locked laser, and both require stabilization to produce a frequency comb, as will be seen below. The first of these is the repetition rate of pulses, f_{rep}, as was discussed previous in chapter 1.2, and the second of these is the so called "carrier envelope offset", or CEO.

The carrier envelope offset, and its related frequency, are related to the fact that within the cavity, due to dispersion, the carrier and envelope do not travel at the same speeds (i.e. $v_g \neq v_\phi$), leading to a phase offset acquired during each round trip of the cavity between the carrier and the envelope's maximal value, as seen in figure 1.7. We refer to the instantaneous difference in phase between the carrier and envelope as the CEO, and the frequency with which the CEO is modulus to f_{rep} as f_{CEO}. This is expressed mathematically in equations 1.18 & 1.17.

$$\Delta\phi_{CEO} \;=\; (\frac{L}{v_g} \;-\; \frac{L}{v_\phi})|_{f_c}\; 2\pi\; f_c \tag{1.17}$$

$$f_{CEO} \;=\; \frac{\Delta\phi_{CEO}\; f_{rep}}{2\pi} \tag{1.18}$$

Where $\Delta\phi_{CEO}$ is the change in carrier envelope offset phase per round trip (and thus between successive pulses), and where v_ϕ and v_g are the average inter-cavity phase and group velocities, respectively, evaluated at the carrier frequency f_c [19].

In this case, $\Delta\phi_{CEO}$ represents an unbounded phase slope. By wrapping the phase change modulo 2π, a limit of $\pm\frac{f_{rep}}{2}$ is applied to f_{CEO}.

In a mode-locked laser, f_{rep} and f_{CEO} govern the frequency of each mode, as seen in figure 1.7 and in equation 1.19, where m is the integer mode index, f_{rep} is the repetition rate as determined by the cavity round trip length, L, and where f_{CEO} is the carrier envelope offset frequency as determined by the difference in inter-cavity phase and group velocities. The following relation has been used for precision frequency metrology with fractional frequency instabilities less than $3e^{-18}$ at 1 second [20] :

$$v_m \;=\; f_{CEO} \;+\; m f_{rep} \tag{1.19}$$

Here, the repetition rate of the pulses, f_{rep}, and the frequency of the carrier envelop offset, f_{CEO}, are held constant. When stabilization is successful, the frequency of each mode is constant over time and can be subsequently referenced to a well known external source [21; 22]. In doing so, the accuracy and stability of the frequency reference is transferred to each tooth and the pulse train as a whole.

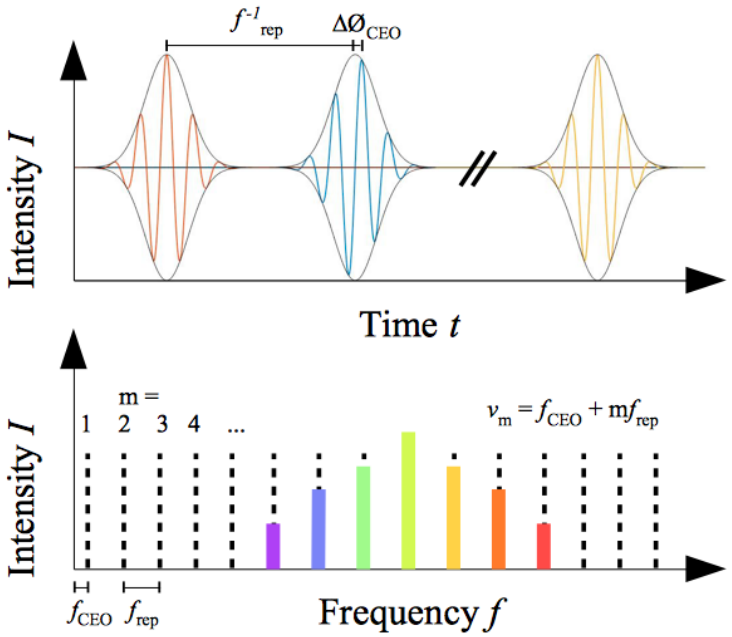

FIGURE 1.7 – A stabilized frequency comb. (top) In the time domain, a pulse train advances with a constant period between each pulse equal to the inverse of f_{rep}, and a constant $\Delta\phi_{CEO}$ between subsequent pulses, as determined by f_{CEO}. (bottom) Mode location is determined by f_{CEO} and f_{rep}. All modes, m, exist, but only some have an associated non-zero intensity, as determined by Fourier transform relations with the time domain signal. In an unstabilized, mode-locked laser, optical modes are free to move, both in terms of translation along the frequency axis, and in terms of frequency spacing between subsequent modes. In our stabilized picture above, modes are locked to a particular frequency. No comb translation, and no breathing are present.

Looking at equation 1.19, it can be seen that an unstable f_{CEO} results in tooth translation along the frequency axis depending on the sign of the change, while an unstable f_{rep} results in the spacing between subsequent comb teeth either increasing or decreasing depending on the sign of the change. The former is referred to as comb translation, while the later is called comb breathing.

Because the repetition rate of the laser is related directly to the cavity length, L, by the equation $f_{rep} = \frac{c}{L}$, the stabilization of the cavity length serves to stabilize the repetition rate. A variety of mechanisms exist to do so, but one common method employs the use of piezoelectric (PZT) materials.

These are a special class of crystalline material which lack inversion symmetry. In layman's terms, this means that the crystalline structure is not symmetric about some central point around which one could invert points to find a mirrored structure on the other side. In such materials, the electric and mechanical states of the crystal may be coupled such that mechanical stress induces an electric charge or vise versa. In the case of cavity length stabilization, the PZT is attached to one cavity mirror, and a voltage is applied which induces a change in its physical dimensions, either shortening or lengthening the cavity. Such a scheme of f_{rep} stabilization is used extensively in my work.

Looking back to equation 1.18, it can be seen that f_{CEO} stabilization depends on two parameters. The first of these is the phase shift acquired per round trip (governed by dispersion), and the second is the repetition rate. To produce a stable f_{CEO}, either both these parameters can be locked to independent values, or both can be changed in unison.

In the case of comb stabilization at both Université Laval and NIST, the pump beam's power is modulated to accomplish this f_{CEO} stabilization [23]. Essentially, the index of refraction of the cavity is changed as a function of input power (see Dr. Newbury's 2005 paper for a full understanding of all those contributing effects) [24; 25]. For now, it will suffice to know that by changing the power in the cavity, we change the dispersion properties of that cavity. This can be done to accomplish either a relative or an absolute CEO lock. Here, by relative locking, we mean that Δf_{CEO} is stabilized between two combs, and by absolute locking we mean that f_{CEO} itself is stabilized.

It remains to be seen, however, how f_{rep} and f_{CEO} stabilization are actually monitored and implemented. Throughout my thesis, I have used two of the most common methods, which will now be discussed further. The first of these methods produces a relative lock between two combs, via the beating of combs against two stabilized continuous wave (CW) references, while the second produces an absolute lock for a single comb via beating against some CW reference in conjunction with "$f \rightarrow 2f$ comparison", as will be discussed below.

The method of relative locking between two frequency combs, as implemented at Université Laval, uses two stable and spectrally narrow CW lasers, with frequencies within the bandwidth of the frequency combs used. By mixing two separate frequency modes from individual combs with a CW laser whose emission frequency is within the combs' bandwidth, an interference pattern can be observed in the radio frequency band which can be directly measured by a photodetector. By analyzing this interference pattern, one can directly measure either the breathing or translation of the individual modes. In our case, corrections are provided via voltage input to a PZT which controls cavity length, and via changes in the pump diode laser current which controls inter-cavity dispersion, ensuring a constant Δf_{CEO} and Δf_{rep} between any two combs [12]. This is discussed in detail in A.2.

An alternative method, employed at NIST, uses an octave spanning comb (a comb which

includes in its spectral bandwidth both some frequency f, and it's frequency double $2f$), broadened via non-linear processes (see section 1.8), to "self-reference", and extract the CEO frequency. This method takes advantage of the fact that, as can be seen from equation 1.19, $f_{CEO} = 2f_m - f_{2m}$. The measurement of f_{CEO} is monitored for stability and controlled by varying the input current of the pump diode. Here, f_{rep} is stabilized by phase locking the comb to a stable CW laser within its bandwidth, and is controlled via both a slow and fast PZT, the first of which has a large range of motion and corrects for slow drifting of cavity length, while the second of which has a shorter dynamic range and corrects for quick changes in cavity length [22].

Once f_{rep} and f_{CEO} are stabilized for a mode-locked laser, we refer to the device as a frequency comb, or simply a comb for short. There are many ways to create a comb, and some of these will be discussed below.

1.5 Types of Frequency Combs

Frequency combs come in many shapes and sizes, but those used in my research fall exclusively under the umbrella of fiber frequency combs. This simply means that the cavity exists within some optical fiber. This not only confines light to a small area which favors non-linear optical effects, but allows for the choice of specialty fiber. For instance, if single-mode, polarization maintaining fiber is chosen, then both polarization and spatial mode interference are well controlled. Mode-locking mechanisms for fiber frequency combs may vary, with some examples already being described including saturable absorbing mirrors, non-linear polarization rotation, and non-linear optical loop mirrors.

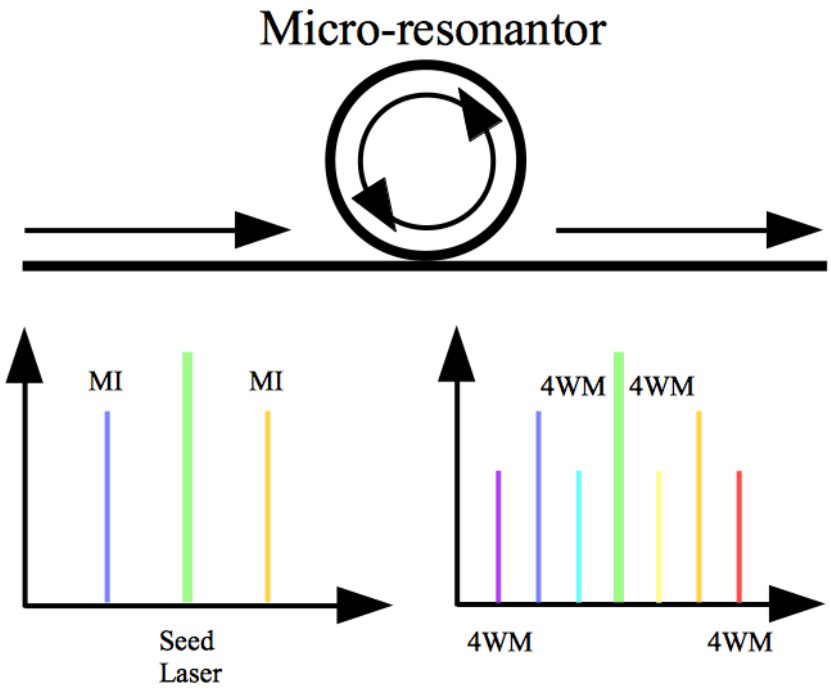

FIGURE 1.8 – A microresonator comb (above) formed by the placement of a resonator near the edge of a leaky waveguide, and (below) the evolution of its spectra. A seed laser is used, which initially produces side frequencies via modulation instability. Various other four wave mixing processes then cascade throughout the spectra, producing a frequency comb, and supporting a single pulse within the resonator.

A second type of frequency comb is created via a microresonantor, and called a microcomb, which is schematically shown in figure 1.8 [26]. In the particular case pictured, both a waveguide and a ring resonator are etched onto some dielectric chip. A single CW or pulsed laser passes through the waveguide while some amount of light is coupled into the resonator. Due to size constraints of the waveguide, and the buildup of light in the microresonator, non-linear optical effects begin to manifest (see section 1.8). These effects initially produce two frequency

lines via modulation instability (MI, a form of degenerate 4 wave mixing), equally spaced on either side of the seed laser. The MI lines then further interact amongst themselves and the seed laser via non-degenerate four-wave mixing to produce cascading, equally spaced spectral lines. In some cases, a single pulse can arise inside the cavity, with an f_{rep} being determined by the effective length of the microresonantor [27]. Such combs tend to have wide tooth spacings, and much higher repetition rates than fiber frequency combs because of their comparatively small cavity lengths.

A third type of frequency comb is an electro-optical comb, which works on the principle of electro-optic modulation of a CW laser via a well known and controllable radio frequency signal [28; 29]. Such a system exploits electro-optical modulators (EOMs) to induce phase/intensity modulation on the seed laser, producing side modes in a cascading fashion. Such a system also offers two independent actuating variables, namely the modulation frequency of the seed laser, and the seed laser frequency itself.

It is worth discussing here a variety of characteristic values of frequency combs. f_{CEO} and f_{rep} have already been discussed, and can be used to find exact tooth location. Other important values include the center optical frequency, the pulse's peak power and duration, the energy per pulse, and the beam's average power. The temporal pulse shape is normally approximated by an equation in order to ease Fourier analysis (Gaussian, sech^2, etc), and the spectral bandwidth of the pulse in the optical domain is measured in wavenumbers, wavelength, or frequency. Common measurements for bandwidth include include the -3db (50% of greatest tooth intensity, FWHM) and the -10db (90% of greatest tooth intensity, FWHM) bandwidth.

1.6 Interferometry

One principle use of frequency combs is in the field of interferometry, a technique in which mutually coherent sources interfere constructively or deconstructively, depending on their phase, onto the surface of a medium used for intensity detection, where the intensity is proportional to the square of the field. This is expressed mathematically in the following equations (equations 1.20 and 1.21), where $U(r,t)$ is the total displacement as a function of location r and time t, of the two summed waves (U_1 and U_2), each having a magnitude of displacement A_x, phase ϕ_x, and angular frequency ω, and where $I(r)$ is the associated intensity.

$$\begin{aligned} U(r,t) &= U_1(r,t) + U_2(r,t) \\ &= A_1(r)e^{i[\phi_1(r)-\omega t]} + A_2(r)e^{i[\phi_2(r)-\omega t]} \end{aligned} \tag{1.20}$$

$$\begin{aligned} I(r) &= \int U(r,t)U^*(r,t)dt \\ &\propto A_1^2 + A_2^2 + 2A_1(r)A_2(r)cos[\phi_1(r) - \phi_2(r)] \end{aligned} \tag{1.21}$$

The resulting pattern in space is referred to as an interferogram (IGM), and contains information about both the intensity, and relative phase of the incoming light. In general, interferogram is used as a broad term referring to any interference pattern in either space or time. An IGM may thus manifest as wave packet, spatial fringe pattern, etc. The instruments which measure and interpret these IGMs are called interferometers, and we divide them into two broad categories, double-path and single-path (or common-path), and provide an example of each.

An example of a double-path interferometer is the Michelson interferometer, used by Albert Michelson [30] in his famously inconclusive experiment that tried to identify the medium into which light is propagating. A typical schematic representation is shown below in figure 1.9.

In a double-path interferometer, a light source is usually split in two by a semi-reflecting, semi-transparent mirror called a beam-splitter. Light then propagates through each of the two arms before being recombined, and is subsequently measured. The two imbalanced arms serve to introduce a differential delay between the recombined fields, called an optical path difference (OPD), which is controllable by moving a mirror in one of the arms, and which can be approximated as a time delay, τ.

The interference pattern produced by a two-beam interferometer, and measured on a photodetector is an estimate of the optical field's autocorrelation function [31], which is described mathematically in equation 1.22 below, where $A(\tau)$ is the autocorrelation function and E represents some complex electric field.

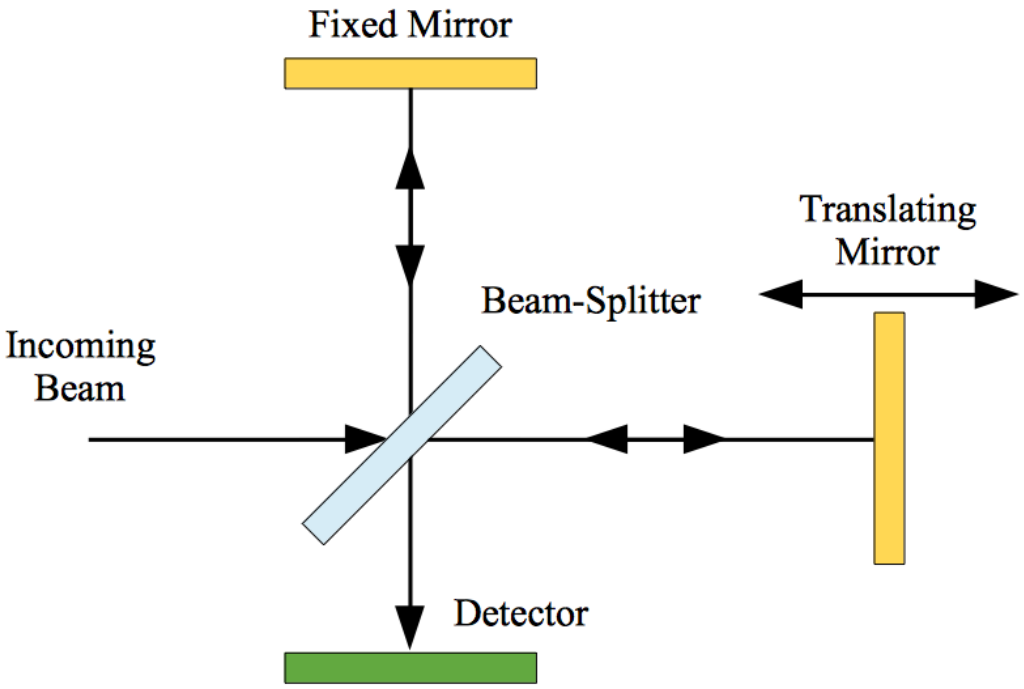

FIGURE 1.9 – A Michelson interferometric setup, consisting of a source laser, a beam-splitter, one fixed mirror, one translating mirror, and a detector. By varying the position of the translating mirror, a source will produce an interference pattern on the surface of the detector. Such a pattern contains all necessary information to determine the relative phase difference between the two beams. Alternatively, a sample may be inserted into the optical setup and the spectral amplitude and phase of the sample's transfer function may be measured.

$$A(\tau) \;=\; \int_{-\infty}^{\infty} E(t)E^{*}(t-\tau)\;dt \tag{1.22}$$

According to the Wiener Khintchine theorem [32], the Fourier transformation of the autocorrelation function is the power spectral density (PSD). Hence, computing the Fourier transform of the interferogram measured as a function of optical path difference, one obtains an estimate of the field's spectrum.

If light is filtered by a sample, in reflection or in transmission, one can extract information about the sample's spectral reflectance or transmittance by making two measurements : one with and one without the sample present in the light path. This is discussed at length in 3.

One example of the single-path or common-path type is the Fabry-Pérot interferometer, also called an etalon [33; 34; 35]. Two typical formats of construction are shown above in figure 1.10. In essence, some portion of a beam passes through the front surface of the etalon, but upon reaching the back surface, partially transmits, and partially reflects. At the front surface, this back reflection partially transmits and partially reflects again. We now have a secondary beam,

which travels along the same path as the initial beam, assuming two flat, parallel surfaces. This process repeats for tertiary beams, etc.

An optical path difference exists between the initial beam and those secondary beams which share a common path with it, meaning that the beam will constructively and deconstructively interfere with its common path back reflections, producing an interferogram which depends upon cavity length. Etalons are particularly important in the context of dual comb spectroscopy, as they are often created accidentally by optical components in the beam's path. This will be discussed further in section 1.7.

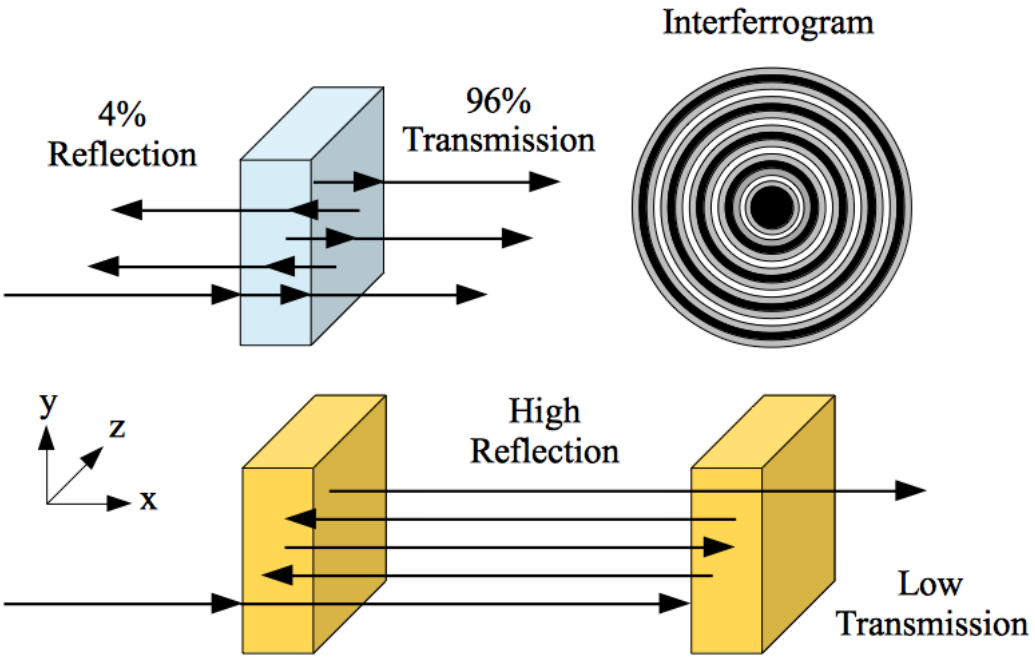

FIGURE 1.10 – A Fabry-Pérot cavity (etalon), in two forms. Each uses a well known fixed distance material (the cavity) to produce an interferogram, one with reflective mirrors and the other relying on fresnel reflections. In the case pictured above, these reflections are between an $n = 1$ material and an $n = 1.5$ material. In the figure above, each reflection is back shifted by a constant z value for ease of visual analysis. In reality, reflections and back-reflections occupy the same physical space assuming parallel, flat reflective surfaces.

Another important distinction among types of interferometry is homodyne vs. heterodyne detection. In homodyne detection, one considers the interference pattern between some source and itself, while heterodyne detection implies that the signal and local oscillator are derived from different sources.

Oftentimes in the field of heterodyne interferometry, one source is well known and under the operator's control. It then serves as a known reference and is called the local oscillator, while the other beam is referred to as the signal.

1.7 Dual Comb Spectroscopy

Dual Comb Spectroscopy (DCS) is an interferometric technique between two frequency combs [36]. The technique is largely based on the fact that any two coherent optical signals with frequencies f_1 and f_2, if spatially overlapped, will interfere to produce two new frequencies, hereafter called heterodyne beats. This is represented mathematically in equation 1.23, where I is the intensity measured after the interference of two E-fields which oscillate in time.

$$\begin{aligned} I &\propto |E_1\cos(f_1 t) + E_2\cos(f_2 t)|^2 \\ &\propto E_1^2\cos^2(f_1 t) + E_2^2\cos^2(f_2 t) + 2E_1E_2 \cdot [\cos(f_1 t)\cos(f_2 t)] \\ &\propto E_1^2\cos^2(f_1 t) + E_2^2\cos^2(f_2 t) + \ E_1E_2 \cdot [\cos((f_1 - f_2)t) + \cos((f_1 + f_2)t)] \end{aligned} \tag{1.23}$$

We can see from the final term of the last expression that this means that one beat will be produced at $f_1 - f_2$ and the other at $f_1 + f_2$. For optical signals, only the difference frequency is accessible for data acquisition, given the high frequency of the sum frequency.

In our case, some stabilized f_{rep} offset Δf_{rep} is introduced between the two combs. Now, assuming two perfect combs, and looking at two teeth (mode numbers m and n), equation 1.24 will describe the location of the difference frequency beat notes.

$$\begin{aligned} \Delta f &= f_1 - f_2 \\ &= f_{CEO,1} + nf_{rep,1} - (f_{CEO,2} + mf_{rep,2}) \\ &= f_{CEO,1} - f_{CEO,2} + nf_{rep,1} + (-nf_{rep,2} + nf_{rep,2}) - mf_{rep,2} \\ &= \Delta f_{CEO} + n\Delta f_{rep} + (n-m)f_{rep,2} \end{aligned} \tag{1.24}$$

Where $\Delta f_{rep} = f_{rep,1} - f_{rep,2}$ and $\Delta f_{CEO} = f_{CEO,1} - f_{CEO,2}$.

We can see that the first two terms of equation 1.24, after being done for all modes, imply the creation of a radio frequency (RF) comb. The first indicates that each mode of the RF comb has a constant frequency offset from zero of Δf_{CEO}, and the second term in the final expression tells us that the modes of this RF comb are separated by Δf_{rep}. Finally, the third term indicates that there is one such comb in each $f_{rep,1} f \approx f_{rep,2} \approx f_{rep}$ interval.

See figure 1.11, and its corresponding caption for a better understanding of this process.

In general, DCS can be done symmetrically, wherein both lasers pass colinearly through the material to be probed, or asymmetrically, wherein only one laser probes the sample(s) under test, while the other is used as a local oscillator to optically sample the sample's impulse response. Both cases are shown in figure 1.12. In the first scenario, the phase response of the sample is imprinted on both combs, and thus drops out in the RF comb. In the asymmetric

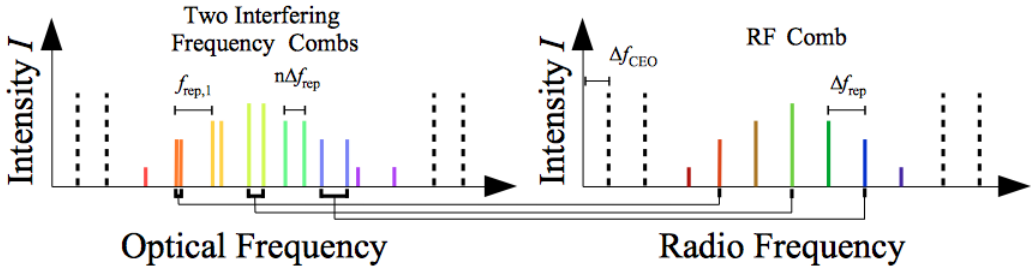

FIGURE 1.11 – (Left) Dual comb spectroscopy in the spectral domain between two combs with a difference in repetition rate Δf_{rep}, showing each of the comb's teeth. Teeth from the first comb interfere with the second comb's teeth to produce an IGM, or RF comb (right) The RF comb, existing within the radio frequency domain, is produced by the interference of two combs with some difference in repetition rate, Δf_{rep}. Connecting lines are drawn between the two interfering modes on the left and their corresponding heterodyne beat on the right.

case, phase data of the local oscillator is conserved, as only the signal beam probes the material. This means that the complex transmittance of the sample can therefore be measured.

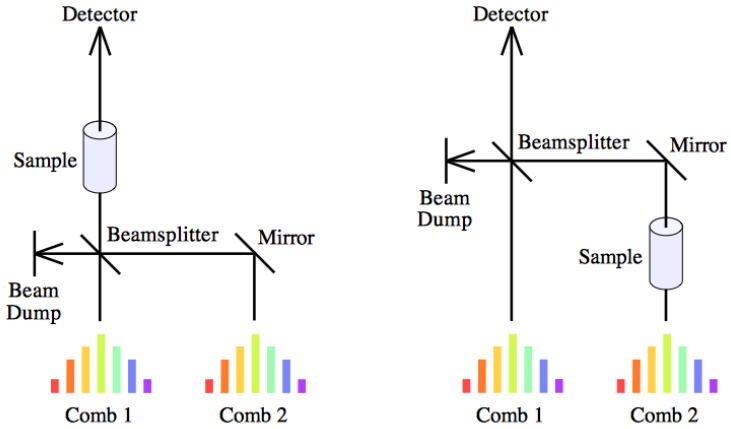

FIGURE 1.12 – (Left) Symmetric dual comb spectroscopy, in which both the local oscillator and signal beams pass colinearly through the sampple (Right) Asymmetric dual comb spectroscopy, in which beam recombination happens after the signal beam has passed through the material. Here, phase data of the local oscillator is conserved, in contrast to the symmetric case, in which it is lost.

An important point should be made here regarding the acquisition of data. In its early days of conception, IGMs gathered from DCS were streamed onto hard drives and treated in post-processing. These days, field programmable gate arrays (FPGAs) are the current first choice due to their ability to phase correct and average subsequent IGMs in real time [12]. Given that signal to noise ratio (SNR) generally grows with the number of IGMs averaged (and thus acquisition time), high SNRs are readily achievable.

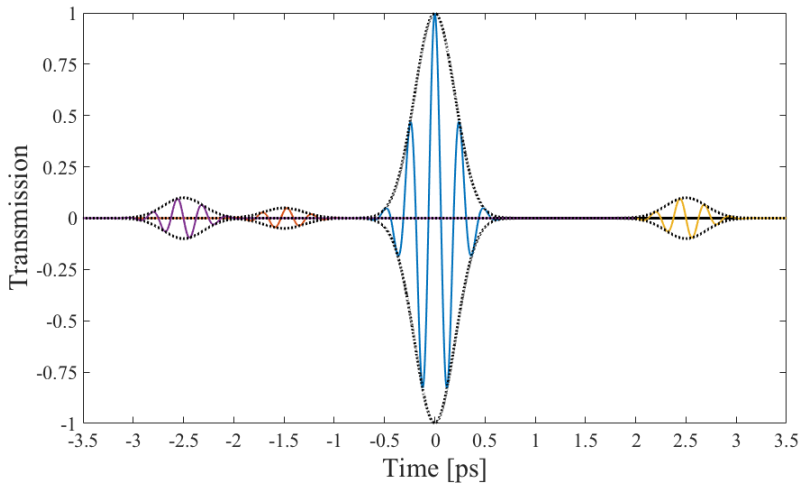

FIGURE 1.13 – Etalons in the time domain. One symmetric etalon exists whose centers are located at ± 2.5 ps. This corresponds to an optical path distance $(n \cdot L)$ of 750 μm, and a modulating frequency on the spectrum of 400 GHz. Its symmetry implies that the etalon appears in both branches (i.e in both the signal and local oscillator) of the interferometer. Another etalon appears at -1.5 ps, corresponding to an optical path distance of 450 μm, which will modulate the frequency spectrum at 667 GHz. The lack of symmetry implies that it exists outside the common path.

It's also worth mentioning here the presence of unintentional interference in dual-comb spectroscopy. Any time a beam passes through a material interface where a change in refractive index occurs, Fresnel reflections are present, with $R = \mid \frac{n_1 - n_2}{n_1 + n_2} \mid^2$ for perpendicular interactions. The process described above in section 1.6, regarding Fabry-Perot interferometers (etalons) occurs, creating a secondary pulse which follows the primary. We refer to these back reflections as etalons.

After the combs interfere on the surface of the detector, etalons manifest as side bursts in the interferogram, either to the left, right, or symmetric about the center (see figure 1.13). In the time domain, etalons are symmetric about the center burst when they are produced after beam recombination, and asymmetric when they occur outside of the common path (see previous section on optical interference).

To better understand the effects of such a side burst, let's look at the addition theorem of Fourier transforms (equation 1.25) and the shift theorem of Fourier transform (equation 1.26).

$$\begin{aligned} FT[f+g](\omega) &= \int_{-\infty}^{\infty} f(t) e^{-i2\pi\omega t} dt + \int_{-\infty}^{\infty} g(t) e^{-i2\pi\omega t} dt \\ &= F(\omega) + G(\omega) \end{aligned} \tag{1.25}$$

$$\begin{aligned} FT[f(t-t_0)](\omega) &= \int_{-\infty}^{\infty} f(t-t_0)e^{-i2\pi\omega t}dt \\ &= F(\omega)e^{-i2\pi\omega t_0} \end{aligned} \tag{1.26}$$

Together, these tell us that a side burst which is a copy of the primary interferogram can be independently Fourier analyzed, and that the result of this analysis is a modulation in the frequency spectra of the center burst corresponding to the delay between the primary and secondary reflections.

Etalons which are closer to the center burst provide a slower (i.e. lower frequency) modulation, while those etalons which are further away provide a faster (i.e. higher frequency) modulation.

Stable etalons may sometimes be referenced out of a measurement via comparison to a "blank" measurement (discussed at length in chapter 3), in which the sample is removed and the interferometer itself is measured. Another common method is via apodization in the time domain (an optical lowerpass filtering technique in which a window function is applied around the center burst). In doing so, special care must be taken, as the choice of window function has a very particular effect on the spectrum [37; 38]. In the frequency domain, this comes at the expense of spectral resolution. Direct downsampling in the frequency domain is also sometimes used, but is not discussed further in this memoire. Ideally, etalons are avoided altogether by removing all parallel surfaces of diffractive media from the optical setup.

1.8 Non-Linear Optics

Broadly speaking, many standard and well known optical processes are non-linear in nature. When we refer to the field of non-linear optics, however, we are often referring to a specific set of processes which occur due to local changes in material polarization state, and which are parametric in nature. By this, we mean that the quantum state of the material is not changed, and as a consequence, the process is "instantaneous" and energy conserving, (i.e. $\Sigma(\hbar\omega_{final}) = \Sigma(\hbar\omega_i)$), where $\hbar$ is the reduced plank's constant and $\hbar\omega$ is the photon energy.

We categorize these processes by their nth order susceptibility term, χ^n, found via the Taylor expansion of the material polarization density equation as a function of electric field (equation 1.27), which is seen in equation 1.28 as a function of time [11].

$$P = \epsilon_0 \chi_e E \tag{1.27}$$

$$P(t) = \epsilon_0 \left(\chi^1 E(t) + \chi^2 E^2(t) + \chi^3 E^3(t) + \ldots\right) \tag{1.28}$$

Where P is the material polarization density (dipole moment per unit volume), ϵ_0 is the permittivity of free space, χ_e is the non-linear susceptibility, E is the applied complex electric field, and χ^n is the n^{th} derivative of χ with respect to the electric field. Here, $\chi^0 = 0$ for all non-ferroelectric materials. All interactions of χ^n produce new frequencies of light, except for when $n = 0, 1$.

For acentrosymmetric crystals (crystals which lack inversion symmetry) χ^2 processes which produce new frequencies of light, like difference frequency generation (DFG), sum frequency generation (SFG), and second harmonic generation (SHG, a degenerate case of SFG), can occur.

To understand, let's suppose that the field is made up of two different frequencies, ω_1 and ω_2. This means we can write the incident field as seen in equation 1.29.

$$E(t) = E_1 e^{i\omega_1 t} + E_1^* e^{-i\omega_1 t} + E_2 e^{i\omega_2 t} + E_2^* e^{-i\omega_2 t} \tag{1.29}$$

This implies that the square of the applied electric field, $E(t)^2$, will have 16 terms, as seen in equation 1.30.

$$
\begin{aligned}
E(t)^2 = & E_1^2 e^{2i\omega_1 t} + E_1^{*2} e^{-2i\omega_1 t} \ldots \text{The second harmonic of } \omega_1 \\
& + E_2^2 e^{2i\omega_2 t} + E_2^{*2} e^{-2i\omega_2 t} \ldots \text{The second harmonic of } \omega_2 \\
& + 2E_1 E_2 e^{i(\omega_1+\omega_2)t} + 2E_1^* E_2^* e^{-i(\omega_1+\omega_2)t} \ldots \text{SFG} \\
& + 2E_1 E_2 e^{i(\omega_1-\omega_2)t} + 2E_1^* E_2^* e^{-i(\omega_1-\omega_2)t} \ldots \text{DFG} \\
& + 2|E_1|^2 + 2|E_2|^2 \ldots \text{Zero frequency - Optical rectification}
\end{aligned} \tag{1.30}
$$

Now, combining equations 1.28 and 1.30, we see that each of these terms will produce some change in the material polarization with a strength according to χ^2. This material polarization is then allowed to oscillate at whatever its frequency happens to be, emitting radiation via Maxwell's equations. In the case of the first two terms of equation 1.30, for instance, the resulting radiation will be the second harmonic of ω_1.

These processes are at their maximum efficiency when the input and output waves have a phase relationship such that all intensity contributions from various points in the crystal are in phase after leaving the crystal. This occurs when the sum of input wave vectors, Σk_i, is equal to the sum of all output wave vectors, Σk_f. The difference between these sums is called the phase matching parameter, and is denoted by Δk.

It's important to keep in mind here, that even for processes such as second harmonic generation, two waves are still interacting to produce a third. In this degenerate case, it just so happens that the two interacting waves are of the same frequency (i.e. $\Delta k = \Sigma k_f - \Sigma k_i = k_{2\omega} - 2k_\omega$). It is for this reason, that χ^2 processes are often considered as 3-wave interactions. This picture is especially useful when considering the problem in terms of the energy conservation of photons.

As a brief example to demonstrate the process, I will discuss the special case of second harmonic generation (which is used in chapter 2). During SHG, a sinusoidally oscillating electric field is applied to some material, which in turn produces a corresponding oscillation (material polarization) in the media. The oscillating electron, however, exists within an anharmonic potential well, and therefore does not oscillate sinusoidally. The non-linear material polarization includes an oscillating contribution at twice the fundamental (seed) frequency, and radiates its own electromagnetic wave outwards via Maxwell's equations. This resultant light is therefore of the second harmonic, or twice the frequency of the input field. This SHG light will be produced at all places within the crystal. When the phase matching condition is not met, however, contributions from various locations in the crystal will not be in phase with one another upon leaving the medium, leading to an overall inefficient conversion scheme [11]

Up until now, our picture of χ has been very limited, assuming a material which has the same response for all directions of excitation and for all frequencies of excitation. In general, this is not the case. Materials are composed of an array of dipoles which are oriented along 3 spatial

directions (x, y, & z), and have different oscillation parameters for each direction, and for each frequency. In reality then, χ^2 must be a 3rd order tensor, with each term evaluated at some ω, as seen in equation 1.31, where subscripts refer to the specific xyz spatial orientation.

$$\chi^2(\omega) \;=\; \begin{pmatrix} \chi^2_{111} & \chi^2_{112} & \chi^2_{113} \\ \chi^2_{121} & \chi^2_{122} & \chi^2_{123} \\ \vdots & \vdots & \vdots \\ \chi^2_{331} & \chi^2_{332} & \chi^2_{333} \end{pmatrix}_{(\omega)} \tag{1.31}$$

Now, keeping in mind that E-fields are directional as well, it becomes obvious that only certain tensor components will be pertinent. It's for this reason that we define an effective non-linear coefficient, d_{eff}, as a sum over only those contributing components after they have been multiplied by a degeneracy factor (set to $\frac{1}{2}$ or 1, depending on whether or not the process is degenerate). As an example, this allows us to write the process of second harmonic generation in a realistic, but simple equation (equation 1.32), commonly found in the literature [39].

$$P^{(2\omega)} \;=\; 2\epsilon_0 \; d_{eff}(2\omega;\omega,\omega) \; |E^{(\omega)}|^2 \tag{1.32}$$

In general, a material's natural phase matching parameter for a given set of frequencies, $\Delta k \; (\omega_1, \omega_2, \omega_3)$ can be used for frequency conversion, but this presents a problem. The efficiency of such a natural phase matching scheme is oscillatory with optical length, having a period $T = \frac{2\pi}{\Delta k}$. This creates a cyclical pattern in the total non-linear frequency generation, and a generally inefficient frequency conversion scheme.

To avoid this, the non-linear crystal's axis can periodically flipped after a distance $d = \frac{T}{2} = \frac{\pi}{\Delta k}$ (see figure 1.14). This inverts the sign of χ for those flipped domains, reversing the loss in efficiency. The total conversion efficiency of the crystal is therefore allowed increase with interaction length, albeit at a slower rate than would be the case for natural phase matching. This is called quasi-phase matching (QPM).

Because of the overall slower efficiency growth, a periodically poled crystal has a d_{eff} which is reduced by $2/\pi$. In contrast, however, it allows for the use of potentially advantageous tensor components of χ^2 by using the same polarization direction for all waves.

For instance, in periodically poled lithium niobate (PPLN), phase matching uses the $d_{31} \;= \sim 4.1 \; pm/V$ component (ignoring the i^{th} term of d_{ijk}, as here we assume interactions are parallel to the Z-axis), while QPM typically uses the $d_{33} \;= \sim 25 \; pm/V$ tensor component, which, even after accounting for efficiency losses due to QPM, is more than 4 times larger, leading to a more efficient frequency conversion scheme overall [40].

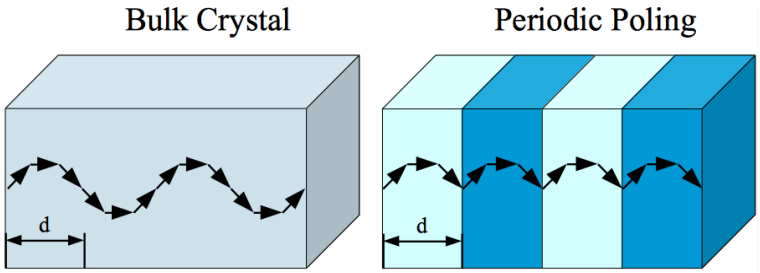

FIGURE 1.14 – A variety of media suitable for non-linear frequency conversion. (left) A bulk crystal, which has a single, set phase matching condition. (right) A periodically poled crystal taking advantage of quasi phase matching conditions from the periodicity of the structure. Here, the arrows represent efficiency of the frequency conversion process.

Let's now examine χ^3 non-linearities, using the general equation 1.33, which solves for the material polarization in a direction i, at a frequency ω_4 [41].

$$P_i(\omega_4) = \frac{1}{4}\epsilon_0 \Sigma_P \Sigma_{jkl} \chi^3_{ijkl}(\omega_4; \omega_1, \omega_2, \omega_3) E_j(\omega_1) E_k(\omega 2) E_l(\omega_3) \tag{1.33}$$

A large variety of four-wave mixing processes fall broadly under the category of χ^3 processes, many of which produce new frequencies of light.

For the purposes of this memoire, however, we're going to focus on a particular manifestation of the χ^3 non-linearity called the Kerr effect. For the most part, the derivation which follows is based on a standard example found in the literature [42].

Let's consider the case where we apply a DC ($\omega = 0$) field $E = \bar{E}$ to some material *while* an optical field with frequency ω propagates through the same medium. We can now write equation 1.33 as equation 1.34 [43].

$$P_i(\omega) = 3\epsilon_0 \Sigma_{jkl} \chi^{Kerr}_{ijkl}(\omega; 0, 0, \omega) \bar{E}_j(0) \bar{E}_k(0) E_l(\omega) \tag{1.34}$$

If we now assume a DC field in the $\hat{y}$ direction, and an optical field which propagates in the $\hat{z}$ direction, then we can write the polarization in the $\hat{x}$ and $\hat{y}$ directions as follows in equations 1.35 and 1.36 respectively.

$$P_x(\omega) = 3\epsilon_0 \chi^{Kerr}_{xyyx}(\omega; 0, 0, \omega) \bar{E}^2_y(0) E_x(\omega) \tag{1.35}$$

$$P_y(\omega) = 3\epsilon_0 \chi^{Kerr}_{yyyy}(\omega; 0, 0, \omega) \bar{E}^2_y(0) E_x(\omega) \tag{1.36}$$

Both these expressions follow the basic form $P(\omega) = C\chi_{eff}E(\omega)$, where C is a constant. We can therefore conclude that there exists some non-linear contribution to the material polarization at ω which is proportional to $\bar{E}^2$. This of course implies a change in the refractive index of the material, and is called the DC-Kerr effect.

The DC-Kerr effect is often presented more succinctly via equations 1.37 & 1.38, where we define Δn as the change in index of refraction due to an excitation at some wavelength λ, K as the Kerr constant, $\bar{E}$ as the applied electric field, n_0 as the intensity independent index of refraction, I as the intensity of incident light, and n_{Kerr} is the so called non-linear index [11].

$$\Delta n \;=\; \lambda K\ \bar{E}^2 \tag{1.37}$$

$$n(I,\lambda) \;=\; n_0(\lambda) \;+\; I \cdot n_{Kerr}(\lambda) \tag{1.38}$$

The DC-Kerr effect, and it's AC counterpart, the optical Kerr effect, are responsible for a wide variety of interesting effects in the field of non-linear optics, just a few of these will be discussed further.

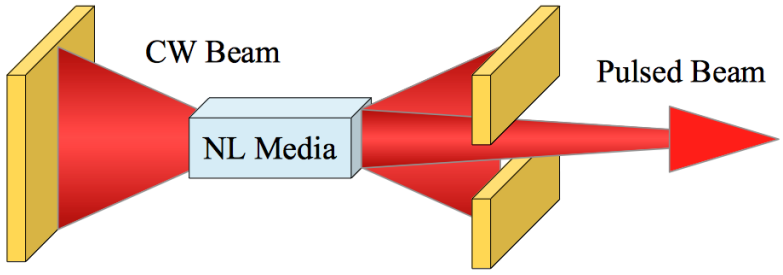

FIGURE 1.15 – Kerr lens mode-locking. Here, a non-linear medium is placed within a laser cavity. Low intensity CW light does not experience lensing, while high intensity light does. Thus, only high intensity (pulsed) light is allowed to leave the cavity.

In the context of self phase modulation, for instance, this Δn produces a variation in the instantaneous phase and therefore the frequency spectrum of the material. This has been shown to be useful in the fields of pulse compression, and supercontinuum generation [44]. The effect can occur *between* wavelengths as well, leading to a phenomenon called cross-phase modulation (XPM), wherein excitation from some incident frequency changes the polarization state of the material and therefore effects the instantaneous phase of light at another frequency [45].

Another consequence of the Kerr effect is self-focusing, in which the intensity dependant index of refraction causes a beam to collapse in upon itself. In essence, a propagating beam will

generally experience radial symmetry in its intensity distribution, with its maximum fluence at its center. Because $n(I) = n_0 + I\ n_{Kerr}$, this produces a lens within the material, focusing the beam into a specific radial pattern, similar to a Gaussian but less stable, called a Towne's profile [46; 47]. This mechanism is useful in a mode-locking scheme called Kerr-lens mode-locking [48], as seen in figure 1.15.

A variety of other, non-parametric processes are contained under the umbrella term non-linear optics as well, such as lasing (which requires a population inversion), two-photon absorption (where the energy of two photons are combined to induce one transition), and saturable absorption (wherein electrons gather in an excited energy band, preventing excitation to that band).

Summary

The chapter begins with basic laser physics and by introducing the concept of resonant modes within the laser cavity. It then moves on to show how a proper fixed phase relationship between these modes can produce a pulsed source, and gives several examples of how to do so, including SESAMS, NOLMs, and NPR.

Next, the Fourier transformation and how it limits the time-bandwidth product of a pulse, a model for including dispersion in the propagation of waves, and finally the Kramers-Kronig relations are all presented.

Next, the actual methods for f_{rep} and f_{CEO} stabilization of a mode-locked laser are discussed, and it is shown how in doing so, a frequency comb is created. A variety of methods for the creation of a frequency comb are discussed. This includes different forms of fiber frequency combs, micro-resonator combs and electro-optical combs.

The field of interferometry is discussed next, focusing on both the single and multi-beam approaches. Having understood the basics of interferometry, we then discuss the actual mechanisms behind dual comb spectroscopy in more detail.

Finally, it is shown how to modify these combs using non-linear optics to expand the technique into new frequency regimes.

Chapitre 2

Pump Probe Dual Comb Spectroscopy

In this chapter, we discuss the results obtained by combining the pump probe technique, which is a technique used for the measurement of time resolved non-linear optics, with dual comb spectroscopy. The resulting instrument offers the ability to quickly measure the complex and time-resolved non-linear response of a system.

The chapter begins by describing the basics of the pump probe technique, and what DCS brings to the table. Then, the materials being used and tested are discussed. This system's functionality, including the working of the FPGA, is validated by repeating the previous results of Julien Roy and JD Deschênes [12]. Finally, a standard SESAM is tested. We measure both the absorbance and phase response in the time domain to non-linear excitation, and compare our data to values as furnished by the manufacturer, BATOP.

2.1 Theory of Pump Probe Dual Comb Spectroscopy

2.1.1 Pump Probe Technique

The goal of pump probe spectroscopy is to measure the non-linear response of a material in the time domain, after that material has been excited by some pulsed source of light [49]. In general, the mechanism of action is as follows : Some high energy pulse (the pump) excites a medium. After some time delay, τ, a secondary pulse (the probe), interacts with the medium (now in its excited state), and is subsequently analyzed [50]. An archetypical layout for such an optical setup (in transmission) is shown in figure 2.1.

Repeating this process for many values of τ allows for the retrieval of time resolved absorption dynamics. This correspond to the medium's excitation and relaxation dynamics. These measurements are highly sensitive to repetition rates, pulse duration, polarization, peak and average powers of the pump beam, chirp of the pulses, solvent used (if the sample is dissolved),

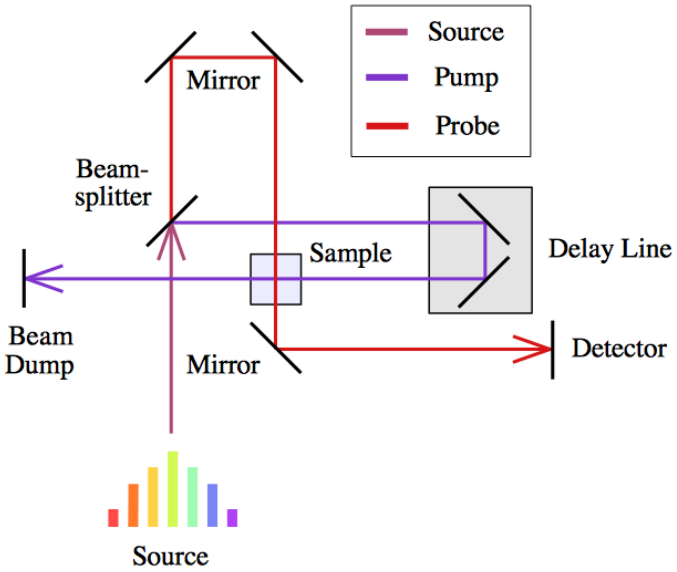

FIGURE 2.1 – A typical layout for pump probe spectroscopy of a transmissive medium. Here, the source beam is split into the pump and probe beams. The pump passes through a delay line, the sample, and finally a beam dump. After some time delay, τ, as determined by the delay line, the probe passes through the sample, and is subsequently measured.

etc [51].

Diverse applications of the technique exist, including the study of laser gain media, inter-band relaxation rates, and many others [52; 53]. One common application for pump probe spectroscopy is the measurement of a saturable absorbing media's relaxation rate. A typical result of such an experiment is shown in figure 2.2.

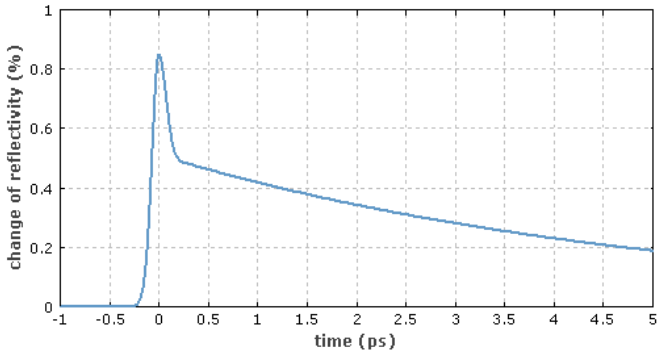

FIGURE 2.2 – The bi-exponential rise and decay of a semiconductor saturable absorbing mirror after being struck with a short, high intensity pulse. Credit RP Photonics.

2.1.2 Pump Probe DCS

While the pump probe technique is useful for measuring the time domain response of a system to various non-linear excitations, it lacks the ability to simultaneously acquire both magnitude and phase spectral information. In combing it with DCS, we achieve all those above capabilities in one system.

An archetypal layout for asymmetric and reflective pump probe dual comb spectroscopy is shown in figure 2.3.

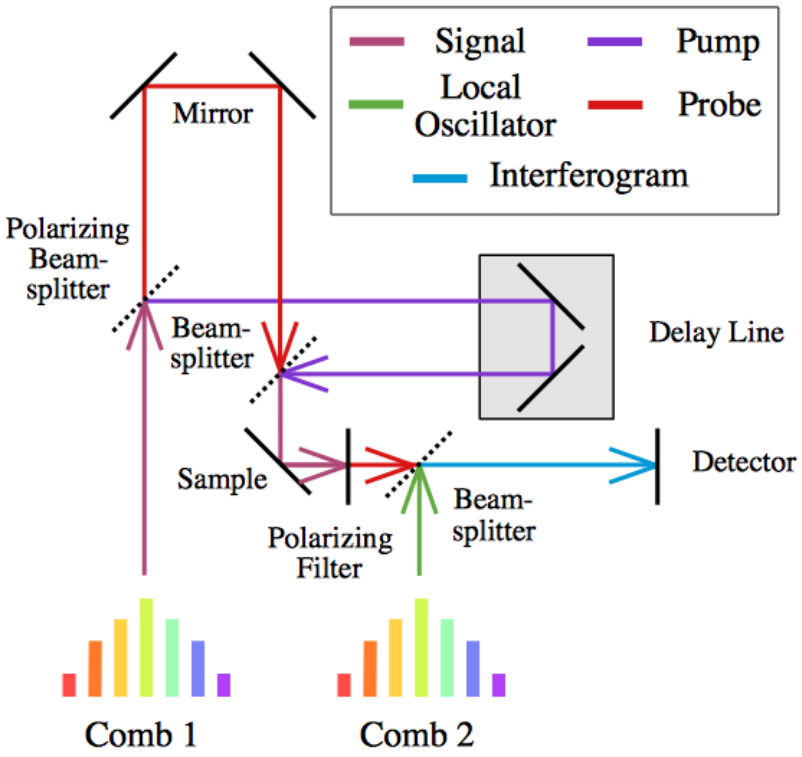

FIGURE 2.3 – The layout of a typical pump probe DCS experiment. The signal beam is split into two, and acts as both the pump and the probe. The pump is sent into a variable delay line, which introduces some time time delay, τ, before exciting the sample. After excitation from the pump, the probe then passes through the sample, and is recombined with the local oscillator, giving us a radio frequency interferogram. IGMs are recorded for many values of τ, yielding the excitation and relaxation dynamics of the sample.

For reflective measurements (pictured), as inspired by the work of Asahara in 2017 [54], the system works as follows : A polarizing beam-splitter divides Comb 1 (the signal) into an s-polarized and p-polarized state, which act as the pump and probe respectively, and which propagate orthogonally. The pump enters a variable delay line, which introduces some time delay τ. The pump and probe beams are then recombined and pass collinearly through the sample. Immediately after interacting with the sample, the pump beam is absorbed by a

polarizing filter. Finally, the probe is combined with Comb 2 (the local oscillator), yielding a radio frequency interferogram.

In most cases, focusing optics are necessary to increase local fluence on the sample and to excite material non-linearities. Aspheric lenses or off-axis parabolas (OAPs) both produce minimal aberrations when used correctly. OAPs, however, are a dispersion free system, and therefore likely to be the ideal focusing optic, despite being difficult to align.

2.2 Verification of DCS System Functionality in the Linear, Steady State Regime

2.2.1 DCS at Université Laval

The pump probe dual comb spectroscopy experiments carried out at Univertsité Laval in Québec, are based on a system first implemented by J. Roy and J-D. Deschênes in 2012 [12]. In order to demonstrate mastery of this system, their results are replicated. Thereafter, the system is expanded to include pump probe functionalities.

To insure the system is fully functional, those results we wish to replicate include the frequency doubling of comb frequencies, the real-time co-adding of successive IGMs, and finally, the spectroscopy of vapor phase rubidium (Rb) in a reference cell.

2.2.2 Materials and Methods for DCS System Functionally Demonstration at Université Laval

Accurate knowledge of reference cell absorption lines are useful for the calibration of tunable diode lasers, stabilization of laser frequencies, and calibration of wavelength meters [55]. They tend to have strong and sharp absorption lines at well known frequencies.

In particular, the test cell used in these initial experiments consists of two rubidium isotopes in their naturally occurring ratio (72.15% ^{85}Rb and 27.85% ^{87}Rb). Each of these isotopes has a $5^2S_{1/2} \rightarrow 5^2P_{3/2}$ transition (called the D_2 line), centered around 780.2412 nm (384 THz), which is well within the bandwidth of a frequency doubled erbium comb.

Rubdium is a group 1 element on the periodic table and thus an alkali metal, which means that its electronic structure falls under roughly the same category as hydrogen. This means that its outermost shell, 5s, contains only a single electron when in the ground state. Within the 5s shell, this single electron is allowed to be in either the spin up, $J = \frac{1}{2}$, or spin down, $J = -\frac{1}{2}$ state, where J is the angular momentum of the electron.

Likewise, the nucleus has an associated spin, I, of either $I = \frac{5}{2}$ for ^{85}Rb, or $I = \frac{3}{2}$ for ^{87}Rb.

This gives us a total atomic angular momentum for the ground state, $F_g = J + I$, of either 2

or 3 for ^{85}Rb , and either 1 or 2 for ^{87}Rb [56]. The cell then, can be thought of as having 4 distinct ground states, each with an associated energy.

While each of these split energy levels is centered about nearly the same frequency, the energy level of each ground state is unique. In ^{85}Rb, for instance, the two ground state energy levels are separated from the center by ± 1.518 GHz, while in ^{87}Rb, they are separated by ± 3.417 GHz [57].

To measure the absorption lines associated with these energy levels, asymmetric dual comb spectroscopy (refer to the previous figure 1.12) is implemented.

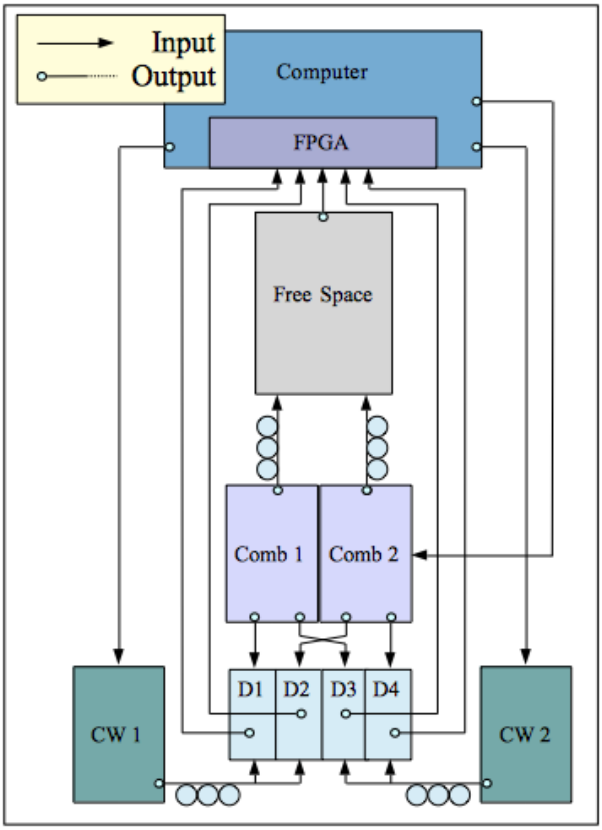

FIGURE 2.4 – Continuous wave frequency references (CW 1, CW 2) mix with the all-fiber combs (Comb 1, Comb 2) on photodiodes to produce 4 signals (D1 - D4). These four signals are sent to an FPGA and used to create 2 reference phase signals, $\Delta\phi_1$ and $\Delta\phi_2$. These reference phases are then used to phase correct and average IGMs in real time. The FPGA also communicates with a top-level MatLab script which serves two functions. The first being to control a servo loop which stabilizes Δf_{rep} and Δf_{CEO} between combs, and the second being to receive and store co-added IGMs from the FPGA.

Both combs are made using erbium doped glass optical fiber, are mode-locked using non-linear polarization rotation, have a pulse reputation rate of approximately 100 Mhz, and come from Menlo Systems. Δf_{rep} between combs is set to 100 Hz. Both Δf_{rep} and Δf_{CEO} are stabilized

between combs as described above in section 1.4.

Before interacting with the sample, both beams are frequency doubled in individual PPLN crystal waveguides. Seed frequencies and their doubles are separated via wedged dielectric mirrors. One frequency doubled beam then passes through a rubidium test cell, before being recombined with the local oscillator (also frequency doubled) in an AR coated, wedged plate beam-splitter. The two collinear beams then interfere on the surface of a silicon detector.

As seen in figure 2.4, along with the IGM, four mixing signals (D1 - D4) are acquired by beating two in-fiber CW reference lasers at 1549.351 and 1562.236 nm against the two frequency combs. All detected signals are then sent to an FPGA which phase corrects and co-adds subsequent IGMs, and which communicates with a top-level MatLab script that manages co-added data and stabilization servo loops.

In short, the goal of detecting the mixing signals D1 - D4 is to use them to find reference phases, $\Delta\phi_1 = D1 \cdot D2^*$ and $\Delta\phi_2 = D3 \cdot D4^*$, which each describe how an individual comb's teeth beat around a single CW reference. These may subsequently be used to align IGMs (necessary for co-adding) [58; 12]. See annex A.2 for a better understanding of this process.

A removal of $\Delta\phi_1$ from the measured IGM removes phase variation between pulses and leaves a corrected signal mapped to a non-uniform optical path distance (OPD) grid. The second correction, the creation of a uniform OPD grid, is then found via subtraction of $\Delta\phi_2$ from $\Delta\phi_1$. A resampling of the now modified IGM on to the new, uniform grid finishes the correction.

A cross-correlation function is applied and monitored in real time in order to align IGMs at a subsample level. A summation of corrected signals is completed over a chosen number, N, of IGMs. A separate Matlab script is then used to either a) manually convert the corrected, uniform OPD grid into an optical frequency (OF) grid using absolute frequency references, such as the spectral spacing between the D_1 and D_2 absorption lines of rubidium as previously reported [59], or b) automatically construct an OF grid using knowledge of the effective sampling frequency and Δf_{rep}. Here we choose the second.

2.2.3 Results of Steady State Rb Spectroscopy

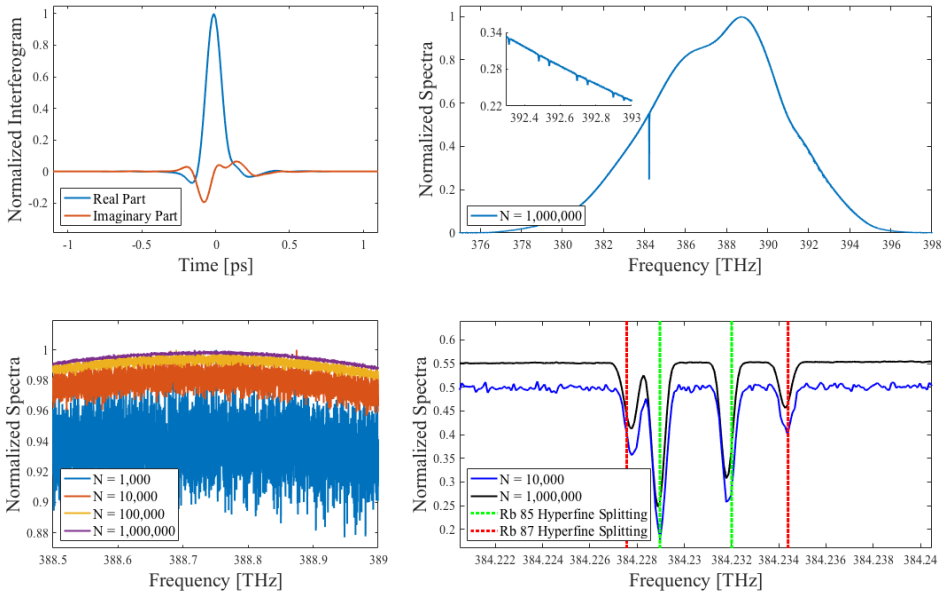

FIGURE 2.5 – (top left) Time domain complex interferogram of the probed Rb cell after corrections and averaging, N = 1,000,000 (∼2.78 hours). (top right) The FT of the complex interferogram to the left, yielding the steady state Rb vapor absorption embedded in the IGM's spectrum. (inset) Zoom-in of oxygen absorption overtones in the near-IR. (bottom left) Demonstration of noise reduction with the number of interferograms averaged, normalized to their maximum respective values. (bottom right) Accuracy of automatic OF grid construction via comparison to known absorption lines of Rb. Two spectra at different N values are shown with a vertical offset to ease comparison.

As seen in figure 2.5, phase correction and coherent addition of successive IGMs via FPGA is successful. After extensive work, the corresponding spectra is largely etalon free, with the amplitude of the strongest etalon being less than 0.2% of the center burst's maximum intensity. For all values of N measured, rubidium's D_2 line is easily resolved. For values of $N > 100,000$, oxygen overtones are visible as well. Quantitatively, we achieve spectral signal to noise ratios of 5.5, 14.6, 20.0, and 21.4 decibels, corresponding to N values of 1,000, 10,000, 100,000 and 1,000,000, respectively. Our OF grid is calculated automatically using knowledge of the effective sampling frequency of the IGM and Δf_{rep}. It can be seen that the maximum error between any point and a known D_2 reference is less than ±200 MHz.

2.3 Time-Resolved Dual Comb Spectroscopy at 1550 nm

2.3.1 Time-Resolved Absorption of a SESAM using Pump Probe DCS

Here we study the time resolved dynamics of a SESAM using pump probe DCS.

In figure 2.6, we see the response of the system to a high energy pulse. A bi-exponential fit is applied to the recovered data points (where each point represents the integrated difference between the spectra at τ and it's $\tau = 0$ counterpart). From this, we find a rise time constant of approximately 5.5 ps, and a relaxation time constant of approximately 23 ps.

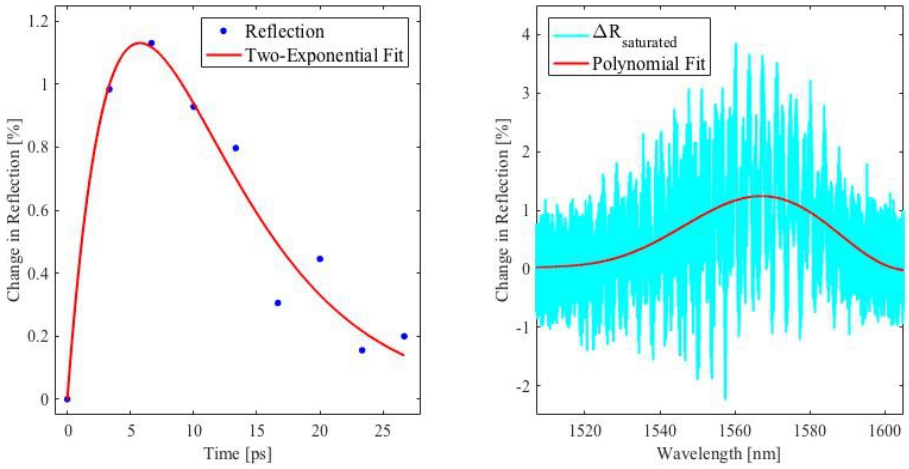

FIGURE 2.6 – (left) Batop SAM spectra integrated from 1510 nm to 1610 nm at various time delays, normalized to data before excitation ($\tau = 0$). (right) Spectral data taken at peak of saturation ($\tau = 6.6$ ps) divided from data taken before excitation (cyan), and subsequently fit using a 4^{th} degree polynomial (red).

In the same figure, we see the saturated state's (corresponding to the data point with the highest modulation depth, $\tau = 6.66$ ps) spectra divided by the acquired spectra at $\tau = 0$. A single, frequency unstable etalon exist between the spectra which is not referenced away after division. A polynomial fit is used to smooth the data pictured, using as justification the fact that the feature in question is quite broad compared the the fast etalon which modulates the spectrum. Here, an aggressive lowpass filter would also be suitable.

This etalon is examined further in figure 2.7. Here, the autocorrelation represents the Fourier transform of the ratio of the saturated and unsaturated states. It's integral then, from $0 \rightarrow \infty$, must represent the total variance between the two spectra in units of transmission. A single delta like peak in the autocorrelation represents a phase and frequency stable etalon, while a wide peak represents either broadband noise or a frequency unstable etalon.

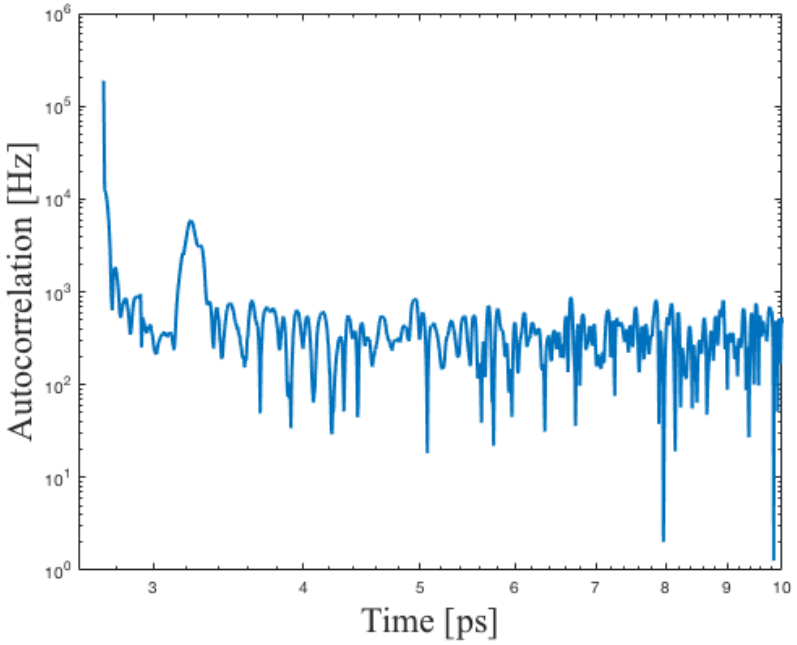

FIGURE 2.7 – The autocorrelation function (IGM space) found by taking the Fourier transform of the ratio of two spectra. The two spectra used are taken from the saturated and unsaturated states.

We note that the associated optical path length for this frequency unstable etalon (at 3.22 ps) is centered at 965 μm, and ranges from 935 μm to 1 mm. The only thing of such a size in the optical setup is the SESAM itself, so we must conclude that the etalon is formed somewhere inside.

All in all, this gives us an effective modulation depth maximum of 1.28% at 1567 nm. This is somewhat smaller than the 2% modulation depth value given by the manufacturer, BATOP, and slightly redshifted from the 1550 nm center claimed. The manufacturer does not give an expected rise time, but does provide a relaxation constant of approximately 20 ps. This matches the value found experimentally.

2.3.2 Phase Response Difference between the Saturated and Unsaturated States of a SESAM using Pump Probe DCS

In figure 2.8, the phase and dispersion response of the medium both before and after excitation to its saturated state is shown. As seen in the panel to the left, the wavelength corresponding to zero phase difference between the saturated and unsaturated states is located at 1550 nm, the claimed center of the SAM's activity. To the right, we see the group velocity dispersion for, and GVD difference between, the saturated and unsaturated states. Each is individually on the order of fs^2, while the difference between them is on the order as^2.

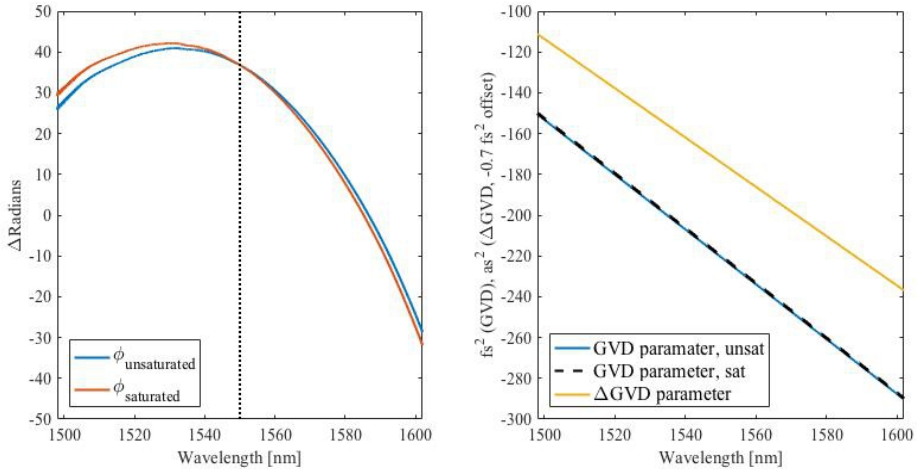

FIGURE 2.8 – (left) Phase data for the unsaturated ($\tau = 0$ ps), state and saturated ($\tau = 6.66$ ps) state, in radians. (right) Group velocity dispersion parameter of the unsaturated and saturated states, in fs^2, as well as the difference between the two, in as^2. An offset of -0.7 fs^2 is applied to the difference spectra to highlight variation between the spectra.

Importantly, the peak modulation depth as seen in figure 2.6 does not correspond to any obvious feature in phase space. This is important, as it suggests phase response stability over the wavelength region for which the SESAM was designed to function.

Summary

In conclusion, we successfully demonstrate mastery of the system set up by Julien Roy and JD Deschênes. We then expand upon this system to include time resolved capabilities by combining the pump probe technique with DCS.

We suggest further studies in which more exotic media are observed, such as carbon nanotubes, graphene saturable absorbers, and the like. Various other studies which take advantage of DCS's spectral resolution would also be very valuable.

Chapitre 3

Experimental Baseline Stability

The results and discussion presented in this chapter correspond to a series of studies on baseline stability. Here, the term baseline is a broad term which refers to any spectral curve which is used as a reference for future measurements.

A stable baseline is not always necessary for the quantitative analysis of dual comb spectra. In fact, the vast majority of DCS experiments have focused on quantitative spectroscopy of narrow absorbers, and simply fit the baseline to a polynomial. In this case, broadband baseline stability is not necessary. On the other hand, a stable baseline *is* necessary for the quantitative analysis of broad absorbers (including solid phase materials). This is the motivation for the chapter.

Various methods of referencing exist to produce a baseline, and the chapter begins by defining some of those methods, and discussing the assumptions of each.

Next, various experimental modifications are studied which can change the baseline. These include multi-path interference, path instabilities, and source variance. Finally, we show how the process of four point referencing can create a stable and flat spectral baseline upon which changes (such as the insertion of a sample) may be observed.

More specifically, the first of these studies focuses on the case of multi-path interference off diffusely scattering surface. The resulting speckle pattern renders the measurement (in general) not useful in a scientifically rigorous manner. Such a measurement simultaneously justifies the interest in further measurements of baseline variance and stability, and demonstrates the need for equivalent optical paths between measurements which are referenced to one another.

Next, we delve deeper into the effect of unstable optical paths. By physically moving the detector relative to the beam, we show that reference curves can be made inaccurate. This serves to highlight the need for optical path stability between successive measurements which

are referenced to one another.

Third, we examine the baseline variance which arises due to the comparison of disparate pulse pairs, and how this is affected by coherent averaging. By having two arms which are referenced to one another but are not delay matched, we are not actually comparing exactly equivalent pulse pairs. Instead, we are comparing intensities which arise due to disparate electric fields. This can be thought of as a variance in each arm's respective source.

Finally, we demonstrate a broadband, four point referenced baseline which is stable over the course of four hours.

3.1 Baselines and Baseline Stability

Let's assume an optical setup which matches that found in figure 3.1, and for which the sample is a transparent glass cell filled with some gas.

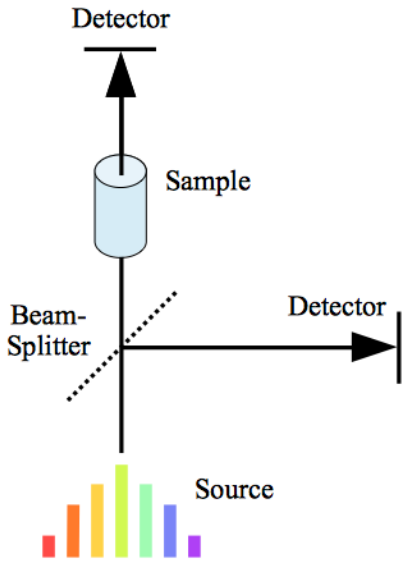

FIGURE 3.1 – An optical setup which is able to measure two paths simultaneously. In one arm (called hereafter the vertical arm), a sample is placed, while in the other (hereafter called the horizontal arm), no sample is present.

Now, if we take a single measurement from the vertical arm (which contains the sample), we are not actually measuring the sample as you might expect. Instead, we are measuring the entire system. This includes the source, optical components such as the beam-splitter, any transparent media (including the gas cell), the atmosphere, the response of the detector, and finally, of course, the sample itself. We are therefore unable to isolate the effect of our sample without taking more measurements, or making a series of assumptions.

Broadly speaking, we consider three methods which attempt to isolate the effect of the sample. The first and second are each a type of two-point referencing, while the third is a combination of the two previous types.

In the first method, called successive referencing, we take two measurements of the vertical arm at different points in time and compare them. One measurement is taken with an empty cell, while the other is taken with a cell full of gas. Successive referencing is appropriate when you know both the source and optical path to be *stable over time*.

In the second method, called simultaneous referencing, we take simultaneous measurements of both the vertical arm (which includes a full gas cell) and the horizontal arm (which includes no cell at all), and then compare these measurements. Simultaneous referencing is appropriate when you know both the source and optical path to be *identical between arms*.

Our final method, called 4 point referencing, is a combination of these techniques. First we take simultaneous measurements of both arms (where the vertical arm has an empty gas cell, and the other has no cell). Then, at a later point, we take simultaneous measurements of the two arms again (this time where the vertical arm contains a cell which is full of gas, and the other has no cell). We then compare the four measurements. 4 point referencing is appropriate when you know the optical path of each arm to be stable over time, and the source to vary identically between arms over time.

We write the electric field at the surface of a detector as a function of the source and some transfer function (i.e. $E_{out} = HE_{in}$), where the transfer function H describes the entire action of the optical path on the source E_{in}, and therefore includes the effects of the sample, atmosphere, detector, path length, etc. Subscripts α and Ω will be used to describe the vertical and horizontal arms respectively. Superscripts of t_0 and t' will be used to describe initial and successive measurements.

The math for successive referencing of the vertical arm is presented in equation 3.1, the math for simultaneous referencing between the vertical and horizontal arms is presented in equation 3.2, and the math for 4 point referencing is presented in equation 3.3. Here, T simply refers to a ratio between two measured signals.

$$\begin{aligned} T_{successive} &= \frac{E^{t'}_{out,\alpha}}{E^{t_0}_{out,\alpha}} \\ &= \frac{H^{t'}_{\alpha} E^{t'}_{in,\alpha}}{H^{t_0}_{\alpha} E^{t_0}_{in,\alpha}} \end{aligned} \tag{3.1}$$

It can thus be seen that we are unable to isolate the sample. In fact, what we measure is every difference in the optical path between time $t = t_0$ and time $t = t'$ (i.e. $\frac{H^{t'}_{\alpha}}{H^{t_0}_{\alpha}}$), as well as

every difference in the source (i.e. $\frac{E^{t'}_{in,\alpha}}{E^{t_0}_{in,\alpha}}$). In order to say with confidence that we're actually observing the impact of the sample with such a measurement, we have to assume that both the source, as well as every portion of the optical path are constant in time (except for the presence of the sample) over the measurement series.

$$\begin{aligned} T_{simultaneous} &= \frac{E^{t_0}_{\alpha,out}}{E^{t_0}_{\Omega,out}} \\ &= \frac{H^{t_0}_{\alpha} E^{t_0}_{\alpha,in}}{H^{t_0}_{\Omega} E^{t_0}_{\Omega,in}} \end{aligned} \tag{3.2}$$

Again, for simultaneous measurements, what we measure is not actually the sample itself. Instead, we're measuring every difference between both arms (i.e. $\frac{H^{t_0}_{\alpha}}{H^{t_0}_{\Omega}}$) at time $t = t_0$, and every difference between the input to each arm (i.e. $\frac{E^{t_0}_{\alpha,in}}{E^{t_0}_{\Omega,in}}$) at time $t = t_0$. In order to say with confidence that we're actually observing the impact of a sample with such a measurement, we have to assume that both sources, as well as every part of the vertical and horizontal arm, are identical (except for the presence of the sample) between arms.

$$\begin{aligned} T_{4point} &= \frac{T^{t'}_{simultaneous}}{T^{t_0}_{simultaneous}} \\ &= \frac{H^{t'}_{\alpha} E^{t'}_{\alpha,in}}{H^{t'}_{\Omega} E^{t'}_{\Omega,in}} \Big/ \frac{H^{t_0}_{\alpha} E^{t_0}_{\alpha,in}}{H^{t_0}_{\Omega} E^{t_0}_{\Omega,in}} \\ &= \frac{H^{t'}_{\alpha} E^{t'}_{\alpha,in} H^{t_0}_{\Omega} E^{t_0}_{\Omega,in}}{H^{t_0}_{\alpha} E^{t_0}_{\alpha,in} H^{t'}_{\Omega} E^{t'}_{\Omega,in}} \end{aligned} \tag{3.3}$$

Here, in order to say with confidence that we are actually measuring the sample, we only have to assume two things. The first assumption is that both optical paths are stable over the course of the measurement in every way (except for the addition of the sample into arm α at some point between the measurements taken at $t = t_0$ and $t = t'$), and the second assumption is that $\frac{E^{t'}_{\alpha,in}}{E^{t_0}_{\alpha,in}} = \frac{E^{t'}_{\Omega,in}}{E^{t_0}_{\Omega,in}}$. In other words, the second assumption is that the input to the vertical arm must vary in the same way as a function of time as the input to the horizontal arm.

To summarize : Successive referencing relies on stability of both the optical path and input source over time. Simultaneous referencing relies on identicality between both the optical path and input source between reference arms. 4 point referencing, on the other hand, relies on the stability of both optical paths over time, and on the input source varying identically in time for each arm (but it does not require the source to be stable over time).

Each of these cases will now be studied.

3.2 Multi-path Interference

To further explore the impact of the optical path, we prepare a simple, symmetric DCS experiment. Here, by symmetric we mean that the local oscillator and signal are combined before passing thru the sample.

Two frequency combs centered each at 1550 nm, with $\Delta f_{rep} = 400$ Hz, are amplified, combined in fiber, collimated after leaving the fiber, and subsequently pass colinearly through an integration sphere (Thorlabs IS200) which is filled with gaseous CO_2. As calculated by Hodgkinson and others, this gives us a total effective pathlength inside the sphere of 1.252 meters, and an average number of 50 scattering events before leaving the cavity [60]. A detector (Thorlabs PDA10CF) is placed near the secondary output of the integration sphere, and an interferogram is measured and co-added for 1 minute (24,000 IGMs).

The topic of etalons (as seen in figure 1.13) has been discussed previously in section 1.7, as one example of unintentional multi-path interference. This topic is expanded upon here and in figure 3.2 to include a diffusely reflective cavity.

Each scattering event inside the sphere will produce many spurious reflections. These then come together to create what is called a speckle pattern, as seen in the top sub-figure of figure 3.2. Such a pattern is characterized by what seems at first glance to be a random (but generally smooth) modulation of intensity, but is in reality the interference between many, many wavefronts. Such a pattern is a typical result of a coherent source being diffusely scattered [61]. The top sub-figure's inset shows the best matching absorption line when compared to a model of the CO_2 absorption based on voigt line shapes and HITRAN parameters, as found from a flat portion of the spectra [62]. Also, seen in the top figure's inset is the chatoic baseline removing the ability to read either an absorption depth, line shape, and line width from an unreferenced spectra.

Pictured in the bottom sub-figure of figure 3.2 is the time domain interferogram corresponding to the spectrum above. In general, it can be said that the presence of distinct peaks here necessitates that some modulating frequency (corresponding to the time delay from the center burst) is present in the spectral domain, although some does come from the free induction decay of CO_2. Unfortunately however, the presence of such side bursts in our IGM does not necessarily imply path stability. Note that the strength of an etalon, for instance, could change over the course of the minute long integration. The spectrum displayed in figure 3.2 shows only the average strength of this etalon.

By physically agitating the sphere, the stability of the path may be sufficiently destroyed such that etalons are effectively turned into white noise, as demonstrated previously [63]. This technique, however, is not applicable to situations where multi-path interference comes from parallel plate Fresnel reflections (etalons).

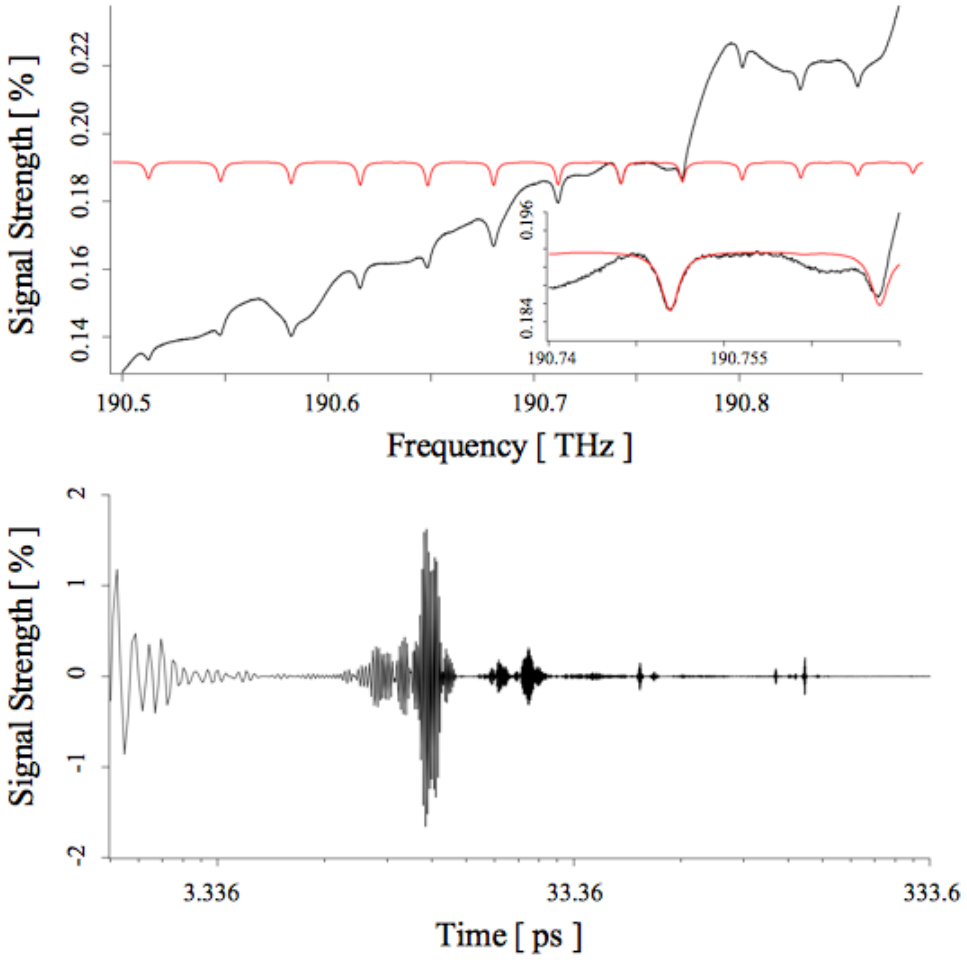

FIGURE 3.2 – (top) Unreferenced, symmetric DCS spectra, normalized to maximum intensity (black) and HITRAN data corresponding to CO_2 lines at standard temperature and pressure, using a 5.7% concentration. (red). A vertical offset is applied to the HITRAN data to highlight line-shape similarities in the flat portions of the spectra, and dissimilarities in portions of the spectra in which the speckle pattern distorts both the line shape and peak location (inset). (bottom) The IGM associated with the spectra above, plotted on a log scale in time to ease comparison with autocorrelation functions which follow.

In general, we can think of the action of the integrating sphere as being an exceptionally complicated transfer function in the context of section 3.1's discussion.

While the case of an integration sphere is admittedly an extreme example of such behavior (etalons in the baseline), the impact of the integration sphere's many diffuse reflections does a good job of highlighting the fact that an unreferenced measurement is generally unable to isolate the effect of the sample (in this case, CO_2). While true that one could conceivably take advantage of CO_2's sharp features and back out some usable data from the pictured spectrum, the quantities in question would be dubious at best.

Moreover, let's consider for a moment the case of simultaneous two point referencing. If one branch of the instrument (say the vertical beam in figure 3.1) were to pick up an etalon (or enter an integration sphere), while the other (horizontal beam) does not, the resulting modulation will be projected onto the baseline. Our final, referenced measurement would include the modulation provided by this etalon (or integration sphere).

3.3 Effect of Changing Beam Position and its Impact on DCS Baseline

Next, to further explore the impact of an unstable optical path, we present a study in which the optical path is purposely changed over the course of multiple measurements.

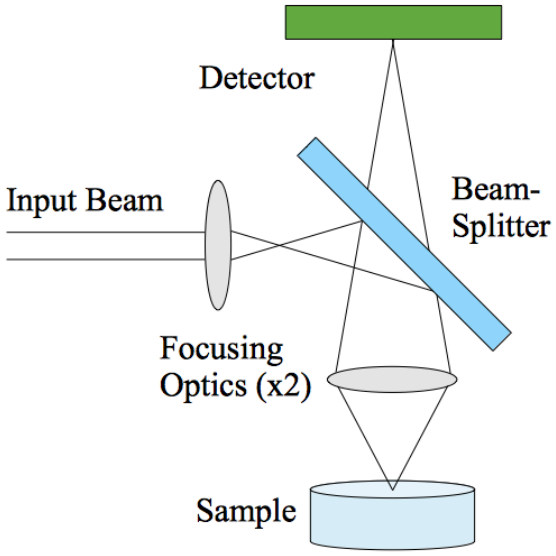

FIGURE 3.3 – A collimated beam is focused, and subsequently sent through a beam-splitter, such that the distance from the focusing optic to the beam-splitter is greater than the focal length of the optic. The first transmitted beam is discarded, while the reflecting beam is focused again, such that the focal point lies on the surface of the sample. The beam which was reflected off the sample now returns to the beam splitter, and transmits onto the surface of the detector. Reflections which are not in focus on the sample are therefore greatly minimized.

Here, we once again combine two erbium combs (Δf_{rep} of 400 Hz) in an all-fiber beam-splitter. The collinear beams are collimated in free space, and pass through a standard confocal microscope (as seen in figure 3.3) and onto the surface of a Thorlabs PDA10CF photodetector. The optical components of this microscope are each less than 1 cm in maximum thickness, AR coated, and are separated in space by increments of 25 mm. A thick (25 mm, 1 inch) window of BK7 is mounted as the sample onto which the microscope is focused. Power on the detector is set to 333 μW for the initial and final measurements, but is allowed to vary between them. The diameter of the beam is measured to be 225 μm in diameter, and the detector surface is μm by 500 μm.

We record a single measurement with the beam located at the center of the detector and call this our zero position. Next, the detector is vertically displaced in increments of 50 μm, and in each case referenced to the center measurement. Finally, after 150 μm of displacement, the detector is returned to its zero position, and a final measurement, also referenced to the first,

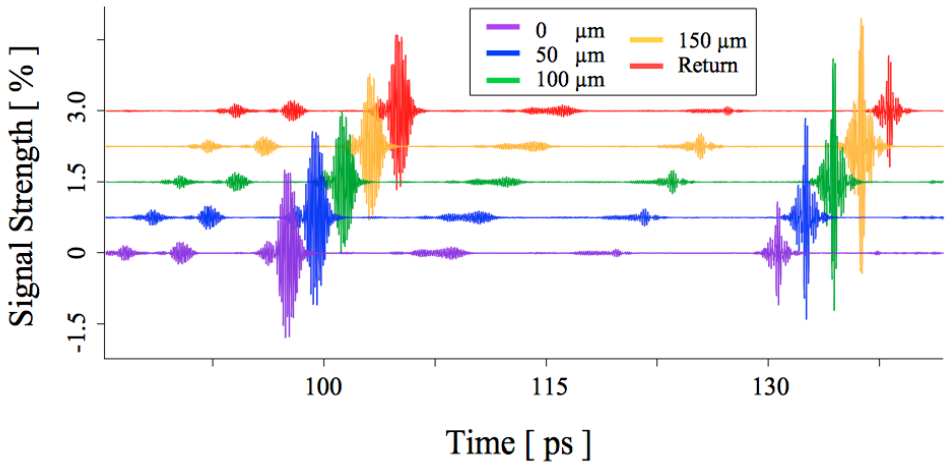

FIGURE 3.4 – Unreferenced Interferograms, normalized to maximum IGM intensity (100 %). The center burst at $t = 0$ is not pictured for any IGM. One IGM is presented for each measurement taken, in the color order in which they were taken (purple → red). Subsequent IGMs are offset in both frequency and time.

is recorded. Unreferenced IGMs for these measurements are presented in figure 3.4, while the referenced measurements in both the transmission and autocorrelation domain are presented in figure 3.5. This represents a two point, successive referencing schema.

In figure 3.4, each IGM is normalized to its maximum intensity. It should be noted, however, that the actual power on the detecter surface decreases as we move further from the initial position, but returns to the initial 333 uW after movement back to the zero position. All etalons are constant between normalized measurements, and drop out after two point referencing, except for one which is located at approximately ± 130 ps. This corresponds to a modulation in the frequency spectrum at approximately 7.7 GHz, and an optical path in vacuum of 3.9 cm or 1.5 inches. Given that the only component in the system which corresponds to such an optical length is the thick glass window used in place of a sample (thickness of 1 inch, $n = 1.5$), it is strongly suggested that this is the source.

In the top panel of figure 3.5, we see the ratio of spectral data taken after movement and spectral data taken at the zero location. As we move further from the center, not only do we acquire a significant tilt to the spectrum (low frequency, unstable noise), we also see the growth of phase and frequency stable noise present at a single frequency (the etalon at ± 130 picoseconds as discussed above).

This is further studied in the bottom subplot, in which we take the Fourier transform of transmission (the FT of the top sub-figure's curves), yielding the autocorrelation function. Here, we see the difference spectra in IGM space, showing only those differences which produce a modulation in the referenced spectra. We see the growth of tilt in the spectral baseline in

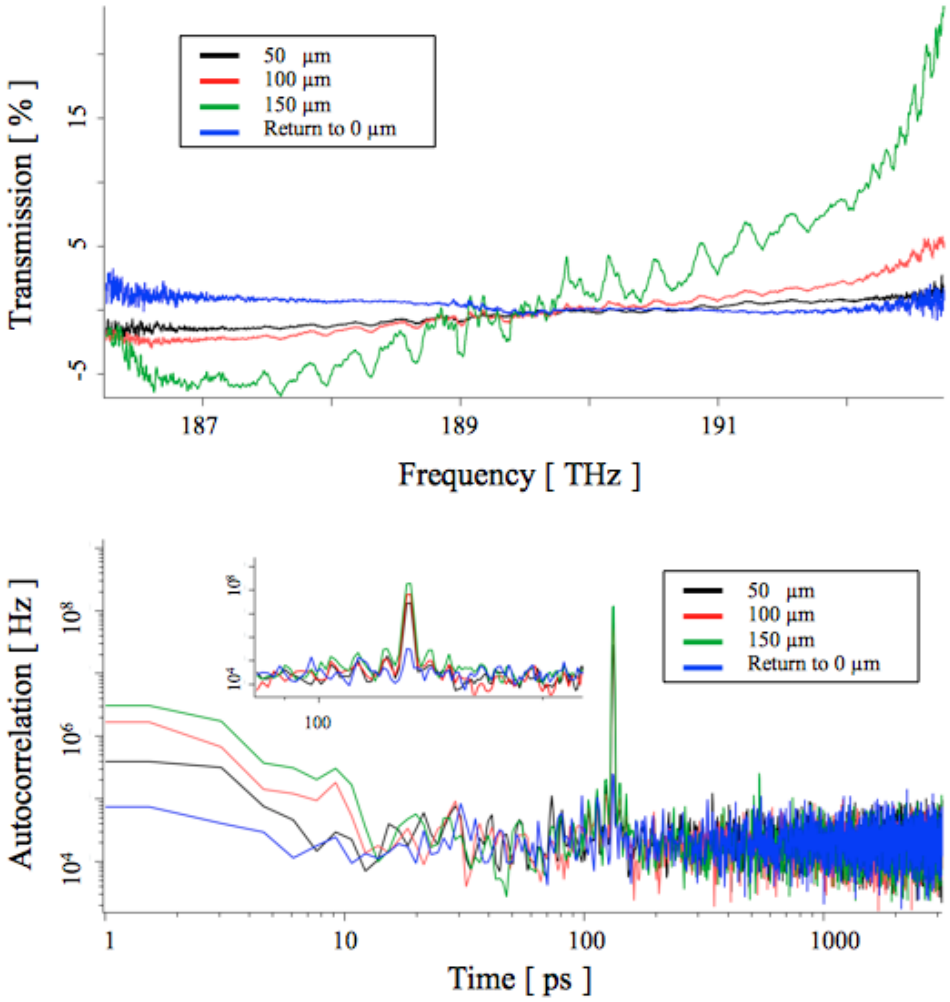

FIGURE 3.5 – (top) Transmission data as found by symmetric DCS after 1 minute of integration. Each curve represents some vertical motion of the detector, in increments of 50 μm, from the center. (bottom) The autocorrelation spectrum, as found by taking the Fourier transform of the above spectra. The inset zooms in on the etalon which changes in intensity with detector movement relative to the beam.

the form of unstable, low frequency noise, as well as the etalon growth at 130 ps.

While likely that the etalon at $\pm$ 130 ps stems from the BK7, and that baseline tilt stems from a change in detector responsivity across the surface [64], neither were the subject of this study, and no definitive claims are made regarding either. Instead, this study serves only to highlight the need for a stable optical path in the context of dual comb spectroscopy (i.e. we show that by changing the transfer function which corresponds to the optical path, we are able to change the output). In this case, we purposely choose a complicated optical setup (a confocal microscope) to highlight the fact that stable etalons may be successfully referenced away after two point referencing.

3.4 Effect of Source Instability on DCS Baseline

Next, we investigate source instabilities and their impact on the baseline of a DCS measurement.

Here, two erbium frequency combs, each individually broadened using highly non-linear fiber (HNLF) are combined in an all-fiber beam-splitter. The resulting symmetric DCS light is collimated into free space, then filtered such that the seed frequency (the orignal comb), and all optical frequencies higher than it are absorbed by the filter. The result is a broad spectrum which spans the wavelength range of 1650-2000 nm.

Now, we return to our initial optical setup, as seen in figure 3.1. Our broadband DCS spectrum is therefore sent into a broadband beam-splitter, and directly onto the surface of two in-house photodetectors. No focusing optics are present, just one beam-splitter and two detectors. The optical paths are not matched in length, and contain no elements besides atmosphere (i.e. two blank paths of unequal length). Δf_{rep} is set to 133 Hz. First, simultaneous two point referencing is done between the two paths over the course of a single second (133 IGMs). Next the same is done over the course of a minute (7980 IGMs). In all cases, power on the detector is estimated to be 333 μW.

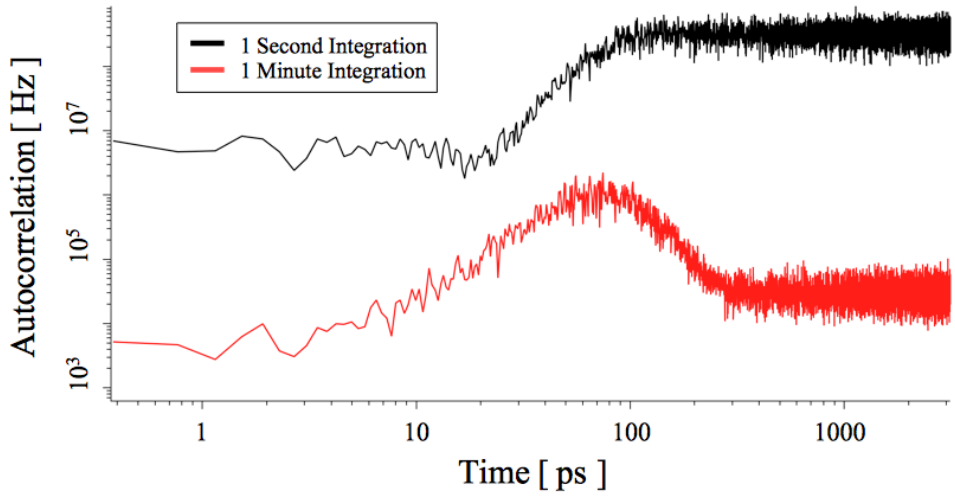

FIGURE 3.6 – The autocorrelation of a one second integration (133 IGMs) after being broadened via HNLF, and the autocorrelation of a one minute integration (7980 IGMs) after being broadened via HNLF. No offset is applied. Spectra are two point referenced to blank paths

This process introduces source variance in two distinct ways. Firstly, it has been well established in the literature that non-linear broadening in HNLFs add additional noise to the spectrum [65; 66]. This can be thought of as non-linear amplification of the pre-existing noise on the seed. Secondly, because no delay matching was done between arms, the simultaneous measurement is actually comparing the intensity of disparate optical fields (although it should

be noted that in general, DCS does assume a train of identical pulses). While both of these points are very interesting in their own right, further comments are outside the scope of this memoire. The important point here being that we are comparing disparate pulse pairs, and that the noise on these pulse pairs has been increased via χ^3 non-linearities during the spectral broadening process.

All this to say that when we take the ratio of our simultaneous measurements (shown in the IGM domain in 3.6), we are not only measuring the difference in optical path (including path length, detector response, etc) but also the source variance between the arms. This difference, in the context of section 3.1's discussion, corresponds to an $E_{in,\alpha}$ and $E_{in,\Omega}$ which are different.

Now, looking again at figure 3.6, we see that two cases are presented (as were described at the beginning of this section), which correspond to a one second integration and a one minute integration. Assuming that both the optical paths and detector response are constant over all measurements taken, we are left to conclude that the only difference we see between the two cases is due to coherent averaging. No further comments are made regarding the impact of coherent averaging on the autocorrelation spectra of referenced measurements. Further analysis into this phenomenon is required, but beyond the scope of this thesis.

3.5 Longterm Baseline Stability in the Context of DCS

Finally, we investigate the long term stability of a broadened DCS measurement.

The same experimental conditions are used here as were used in section 3.4, except for a few modifications. First, a simultaneous measurement is taken between the two arms, and co-added over a period of 20 minutes (159,600 IGMs). Immediately after, while holding all other variable constant, another 20 minute integration is performed. This continues for 4 hours, with every measurement besides the first being referenced to the first. We therefore have both successive and simultaneous measurements - or 4 point referencing.

It is also important to highlight that for these measurements, power on the detector was set to approximately 80 μW, such that the total noise (which can be found by integrating the autocorrelation from $0 \rightarrow \infty$) is significantly elevated.

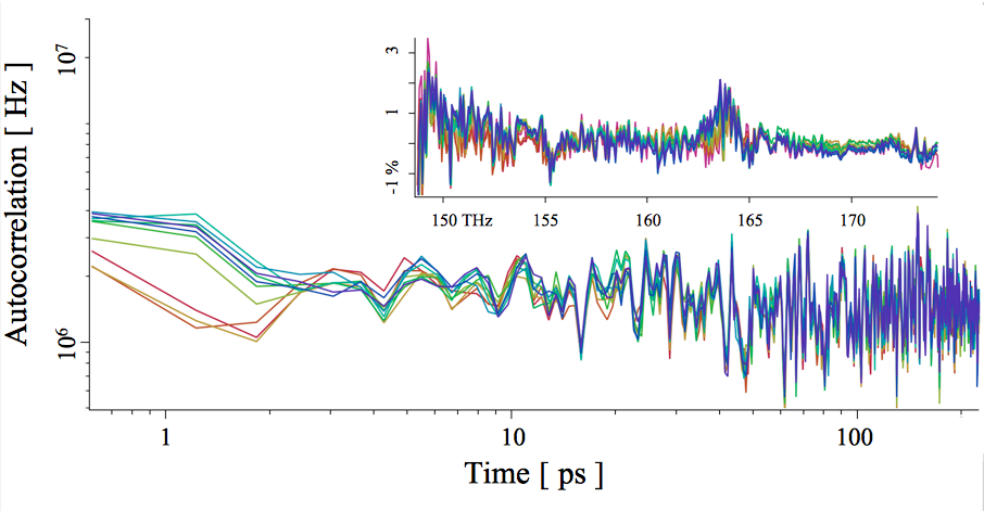

FIGURE 3.7 – The autocorrelation of baseline stability over the course of four hours, where each color represents a successive 20 minute integration as four point referenced to both a blank measurement and some measurement at $t = 0$. (inset) The corresponding transmission spectra ($T = \frac{\text{arm 1}}{\text{arm 2}}$) for each curve, before being four point referenced to the measurement at $t = 0$.

This is all shown in figure 3.7, where we track the four point referenced autocorrelation along with the two point referenced transmission spectra over the course of 4 hours.

For the first time in this memoire, the autocorrelation spectra are largely flat as a function of time. This implies that all etalons (which would manifest as sharp, pronounced peaks in the autocorrelation function) have been referenced away, and that no tilt (which has been shown to manifest as low frequency, broadband noise) is accumulated in the frequency spectrum over the course of the measurement

Indeed, looking at the largest change in transmission at any single frequency over the course

of 4 hours, we observe a maximum difference of approximately 1%. Such a stable baseline is required for spectroscopy of broad absorbers.

Summary

In the preceding chapter, we define and implement various ways to reference spectra, and discuss the implications of each.

We show that DCS is achievable after many diffuse reflections (and thus significant speckle / multi-path interference), but that the data recovered must be properly referenced before being rigorously useful in a scientific context.

We also show that that movement of the detector relative to the beam can introduce significant tilt to a spectrum, which manifests in the autocorrelation spectrum as broadband low frequency noise. This process is also shown to be reversible. We believe this to have a variety of implications, especially concerning long path open air measurements which have been shown to be sensitive to turbulent atmospheric conditions.

Finally we demonstrate that coherent averaging is able to change the noise curve in the autocorrelation domain (i.e. different portions of the autocorrelation spectrum are affected differently by the process) in the case of simultaneous referencing of disparate pulse pairs. Currently, we lack both a model and the data to definitively explain this behavior.

We also achieve a broadband DCS baseline which is stable over the course of 4 hours, as measured via 4 point referencing.

Conclusion

In conclusion, three topics are discussed.

The first chapter focuses on theory. This includes the basic physics of lasers, mode-locking, f_{rep} and f_{CEO} stabilization, interferometry, DCS, and non-linear optics. This not only demonstrates a mastery of the subject, but also provides the reader with all necessary information required for the understanding of subsequent chapters.

The second chapter focuses on the combination of DCS with the well known pump-probe technique. This chapter begins with an explanation of pump-probe spectroscopy, and what frequency combs add to the technique. Next, previous measurements are replicated to demonstrate mastery of the system and verify its functionality. Finally, the system is expanded upon to include time domain functionality. Pump probe DCS results are then presented and analyzed.

The last chapter focuses on the analysis of spectral baseline variance. A mathematical model is developed to better understand various referencing techniques. Then, various experimental modifications are performed, each of which highlights the assumptions underlining various referencing techniques. Examples of these changes include optical path instability, source variance, etc. Finally, a stable four point referenced measurement is shown over the course of four hours.

All combined, a mastery of the theory of DCS, an ability to use and expand upon the technique, and the ability to explore its fundamental assumptions are each demonstrated.

Annexe A

Derivations

A.1 Derivation of the Kramers-Kronig Relations

This derivation largely follows a common method described by M. Schonleber [67]. We begin with an impulse response function of a linear system which is invariant in time, $h(t)$.

The frequency response is therefore expressed as $H(\omega)$, as seen in equation A.1.

$$H(\omega) = \frac{1}{\sqrt{2\pi}} \int_{-\infty}^{\infty} h(t) e^{-i\omega t} dt \qquad \text{[By Fourier transformation (FT)]} \quad \text{(A.1)}$$

Knowing that the impulse response is equal to 0 for all times $t < 0$ from causality, and assuming it is non-zero for times $t > 0$, $h(t)$ must obey the equality found in equation A.2, where $\sigma(t)$ is the Heaviside step function.

$$h(t) = \sigma(t)h(t) \qquad \text{[By causality]} \quad \text{(A.2)}$$

We now take the Fourier transform of $h(t) = \sigma(t)h(t)$, as seen in equation A.4.

$$F[h(t) \cdot \sigma(t)] = \frac{1}{\sqrt{2\pi}} H(\omega) * F[\sigma(t)] \qquad \text{[By the convolution theorem]} \quad \text{(A.3)}$$

$$= H(\omega) * \left\{ \frac{1}{2\pi} \left[\frac{1}{i\omega} + \pi\delta(\omega) \right] \right\} \qquad \text{[FT of the Heaviside step function]} \quad \text{(A.4)}$$

Now, we remember what a convolution means, as seen in equation A.5.

$$[f * g](\omega) = \int_{-\infty}^{\infty} f(\omega') g(\omega - \omega') d\omega' \qquad \text{[Definition]} \quad \text{(A.5)}$$

Following some simplification, we can therefore write equation A.4 in a new form, as seen below in equation A.8.

$$H(\omega) = \frac{1}{2\pi}\left\{\int_{-\infty}^{\infty}\frac{H(\omega')}{i(\omega-\omega')}d\omega' + \int_{-\infty}^{\infty}\pi H(\omega')\delta(\omega-\omega')d\omega'\right\} \tag{A.6}$$

$$= \frac{1}{2\pi}\left\{\int_{-\infty}^{\infty}\frac{H(\omega')}{i(\omega-\omega')}d\omega' + \pi H(\omega)\right\} \tag{A.7}$$

$$= \frac{1}{\pi}\int_{-\infty}^{\infty}\frac{H(\omega')}{i(\omega-\omega')}d\omega' \quad \text{[Simplification]} \tag{A.8}$$

From here, we separate the integral $-\infty \to \infty$ into two parts as follows in equation A.9.

$$\int_{-\infty}^{\infty}\frac{H(\omega')}{i(\omega-\omega')}d\omega' = \int_{-\infty}^{0}\frac{H(\omega')}{i(\omega-\omega')}d\omega' + \int_{0}^{\infty}\frac{H(\omega')}{i(\omega-\omega')}d\omega' \quad \text{[By linearity of integration on } \mathbb{R}\text{]} \tag{A.9}$$

Next, we rewrite the integral $-\infty \to 0$ such that it can be combined with the positive integration. This is shown in equation A.10.

$$\int_{-\infty}^{0}\frac{H(\omega')}{i(\omega-\omega')}d\omega' = \int_{0}^{\infty}\frac{H(-\omega'')}{i(\omega+\omega'')}d\omega'' \quad \text{[Redefinition of } \omega'\text{]} \tag{A.10}$$

Now, because the Fourier transform of a real signal is guaranteed to be Hermitian, $H(-\omega'') = H^*(\omega'')$, and we rewrite equation A.9 as follows in equation A.13.

$$H(\omega) = \frac{1}{\pi}\left\{\int_{0}^{\infty}\frac{H(\omega')}{i(\omega-\omega')}d\omega' + \int_{0}^{\infty}\frac{H^*(\omega'')}{i(\omega+\omega'')}d\omega''\right\} \tag{A.11}$$

$$= \frac{1}{\pi}\int_{0}^{\infty}\frac{H(\omega')\cdot(\omega+\omega') + H^*(\omega')\cdot(\omega-\omega')}{i(\omega^2-\omega'^2)}d\omega' \tag{A.12}$$

$$= \frac{2}{\pi}\int_{0}^{\infty}\frac{H_{Im}(\omega')\cdot\omega' - iH_{Re}(\omega')\cdot\omega}{\omega^2-\omega'^2}d\omega' \quad \text{[Separation of complex components]} \tag{A.13}$$

And finally, by splitting up the real and imaginary parts of the final expression found in equation A.13, we arrive at the standard expressions for the Kramers-Kronig relations as seen in equations A.14 and A.15.

$$H_{Re}(\omega) = \frac{2}{\pi}\int_{0}^{\infty}\frac{\omega' H_{Im}(\omega')}{\omega^2-\omega'^2}d\omega' \tag{A.14}$$

$$H_{Im}(\omega) = \frac{-2}{\pi} \int_0^\infty \frac{\omega H_{Re}(\omega')}{\omega^2 - \omega'^2} d\omega' \tag{A.15}$$

A.2 Relative Locking at Université Laval

In order to lock Δf_{rep} and Δf_{CEO} of the system used at Université Laval, two CW lasers are employed as intermediary oscillators.

Each one (CW_1 and CW_2) has an associated power (P_{CW_1} and P_{CW_2}), frequency (f_{CW_1} and f_{CW_2}), and phase (ϕ_{CW_1} and ϕ_{CW_2}).

Each comb (FC_1 and FC_2) has an associated power about each CW laser frequency ($P_{FC_1,f_{CW_1}}$, $P_{FC_1,f_{CW_2}}$, $P_{FC_2,f_{CW_1}}$, and $P_{FC_2,f_{CW_2}}$), center frequency (f_{FC_1} and f_{FC_2}), phase (ϕ_{FC_1} and ϕ_{FC_2}), and delay between pulses (T_{FC_1} and T_{FC_2}).

The measured signals D1 - D4 then, can be expressed as seen in equations A.16, A.17, A.18, and A.19, as a function of k, the index of a pulse pair.

$$D1(k) = \sqrt{P_{CW_1} P_{FC_1,f_{CW_1}}} \cdot e^{\{i2\pi f_{CW_1} T_{FC_1}(k) + i\phi_{FC_1}(k) + i\phi_{CW_1}(T_{FC_1}(k))\}} \tag{A.16}$$

$$D2(k) = \sqrt{P_{CW_1} P_{FC_2,f_{CW_1}}} \cdot e^{\{i2\pi f_{CW_1} T_{FC_2}(k) + i\phi_{FC_2}(k) + i\phi_{CW_1}(T_{FC_2}(k))\}} \tag{A.17}$$

$$D3(k) = \sqrt{P_{CW_2} P_{FC_1,f_{CW_2}}} \cdot e^{\{i2\pi f_{CW_2} T_{FC_1}(k) + i\phi_{FC_1}(k) + i\phi_{CW_2}(T_{FC_1}(k))\}} \tag{A.18}$$

$$D4(k) = \sqrt{P_{CW_2} P_{FC_2,f_{CW_2}}} \cdot e^{\{i2\pi f_{CW_2} T_{FC_2}(k) + i\phi_{FC_2}(k) + i\phi_{CW_2}(T_{FC_2}(k))\}} \tag{A.19}$$

Next, these signals are used to find two referenced signals R_1 and R_2, as seen in equations A.20 and A.21.

$$\begin{aligned} R_1 &= D1 \cdot D2^* \\ &= P_{CW_1} \sqrt{P_{FC_1,f_{CW_1}} P_{FC_2,f_{CW_1}}} \cdot e^{\{i2\pi f_{CW_1}\Delta T(k) + i\Delta\phi(k) + i\phi_{CW_1}(T_{FC_1}(k)) - i\phi_{CW_1}(T_{FC_2}(k))\}} \end{aligned} \tag{A.20}$$

$$\begin{aligned} R_2 &= D3 \cdot D4^* \\ &= P_{CW_2} \sqrt{P_{FC_1,f_{CW_2}} P_{FC_2,f_{CW_2}}} \cdot e^{\{i2\pi f_{CW_2}\Delta T(k) + i\Delta\phi(k) + i\phi_{CW_2}(T_{FC_1}(k)) - i\phi_{CW_2}(T_{FC_2}(k))\}} \end{aligned} \tag{A.21}$$

To phase correct the incoming interferogram, we normalize R_1^* and multiply it by the IGM. This leaves a corrected signal mapped to a non-uniform OPD grid.

To map the IGM to a uniform OPD grid, we need only extract the phase difference between the two referenced signals, *i.e.* $R_1^*(k) \cdot R_2(k)$.

Finally, we find the effective optical sampling frequency, as given by the FPGA, along with the number of data points in our IGM, and subsequently produce an optical axis.

A full derivation of the process is seen in J.-D. Deschênes' 2010 paper [58].

Bibliographie

[1] A.E. Siegman. *Lasers*. University Science Books, 1986.

[2] Sara R Hastings-Simon, Matthias U Staudt, Mikael Afzelius, Pascal Baldi, Didier Jaccard, Wolfgang Tittel, and Nicolas Gisin. Controlled stark shifts in er3+-doped crystalline and amorphous waveguides for quantum state storage. *Optics communications*, 266(2) :716–719, 2006.

[3] Seppo Honkanen, Tomoko Ohtsuki, Shibin Jiang, S Iraj Najafi, and Nasser Peyghambarian. High er concentration phosphate glasses for planar waveguide amplifiers. In *Rare-Earth-Doped Devices*, volume 2996, pages 32–41. International Society for Optics and Photonics, 1997.

[4] Danny G O'shea, Jonathan Ward, Brian Shortt, Michel Mortier, Patrice Feron, and Nic Chormaic. All taper coupled microspherical light source. *OSA*, 10 2007.

[5] Gaozhong Wang, Kangpeng Wang, Beata M Szydłowska, Aidan A Baker-Murray, Jing Jing Wang, Yanyan Feng, Xiaoyan Zhang, Jun Wang, and Werner J Blau. Ultrafast nonlinear optical properties of a graphene saturable mirror in the 2 um wavelength region. *Laser and Photonics Reviews*, 11(5) :1700166, 2017.

[6] Ursula Keller, Kurt J Weingarten, Franz X Kartner, Daniel Kopf, Bernd Braun, Isabella D Jung, Regula Fluck, Clemens Honninger, Nicolai Matuschek, and J Aus Der Au. Semiconductor saturable absorber mirrors (sesam's) for femtosecond to nanosecond pulse generation in solid-state lasers. *IEEE Journal of selected topics in QUANTUM ELECTRONICS*, 2(3) :435–453, 1996.

[7] Xinhuan Feng, Hwa-yaw Tam, and PKA Wai. Stable and uniform multiwavelength erbium-doped fiber laser using nonlinear polarization rotation. *Optics express*, 14(18) :8205–8210, 2006.

[8] Jan Szczepanek, Tomasz M Kardaś, Czesław Radzewicz, and Yuriy Stepanenko. Nonlinear polarization evolution of ultrashort pulses in polarization maintaining fibers. *Optics express*, 26(10) :13590–13604, 2018.

[9] ME Fermann, MJ Andrejco, Y Silberberg, and ML Stock. Passive mode locking by using nonlinear polarization evolution in a polarization-maintaining erbium-doped fiber. *Optics letters*, 18(11) :894–896, 1993.

[10] NJ Doran and David Wood. Nonlinear-optical loop mirror. *Optics letters*, 13(1) :56–58, 1988.

[11] Peter E Powers and Joseph W Haus. *Fundamentals of nonlinear optics*. CRC Press, 2017.

[12] Julien Roy, Jean-Daniel Deschênes, Simon Potvin, and Jérôme Genest. Continuous real-time correction and averaging for frequency comb interferometry. *Optics express*, 20(20) :21932–21939, 2012.

[13] David L Donoho and Philip B Stark. Uncertainty principles and signal recovery. *SIAM Journal on Applied Mathematics*, 49(3) :906–931, 1989.

[14] P Lazaridis, G Debarge, and P Gallion. Time–bandwidth product of chirped sech 2 pulses : application to phase–amplitude-coupling factor measurement. *Optics letters*, 20(10) :1160–1162, 1995.

[15] Linn F Mollenauer and James P Gordon. *Solitons in optical fibers : fundamentals and applications*. Elsevier, 2006.

[16] Olga Krivokhvost et al. Conventional and nonconventional kramers-kronig analysis in optical spectroscopy. 2014.

[17] Valerio Lucarini, Jarkko J Saarinen, Kai-Erik Peiponen, and Erik M Vartiainen. *Kramers-Kronig relations in optical materials research*, volume 110. Springer Science & Business Media, 2005.

[18] Craig F Bohren. What did kramers and kronig do and how did they do it ? *European Journal of Physics*, 31(3) :573, 2010.

[19] Jun Ye and Steven T Cundiff. *Femtosecond optical frequency comb : principle, operation and applications*. Springer Science and Business Media, 2005.

[20] Holly Leopardi, Josue Davila-Rodriguez, Franklyn Quinlan, Judith Olson, Jeff A Sherman, Scott A Diddams, and Tara M Fortier. Single-branch er : fiber frequency comb for precision optical metrology with 10- 18 fractional instability. *Optica*, 4(8) :879–885, 2017.

[21] Christoph Gohle, Thomas Udem, Maximilian Herrmann, Jens Rauschenberger, Ronald Holzwarth, Hans A Schuessler, Ferenc Krausz, and Theodor W Hänsch. A frequency comb in the extreme ultraviolet. *Nature*, 436(7048) :234, 2005.

[22] Laura C Sinclair, J-D Deschênes, L Sonderhouse, William C Swann, Isaac H Khader, Esther Baumann, Nathan R Newbury, and I Coddington. Invited article : A compact optically coherent fiber frequency comb. *Review of scientific instruments*, 86(8) :081301, 2015.

[23] FW Helbing, G Steinmeyer, J Stenger, HR Telle, and U Keller. Carrier–envelope-offset dynamics and stabilization of femtosecond pulses. *Applied Physics B*, 74(1) :s35–s42, 2002.

[24] Nathan R Newbury and Brian R Washburn. Theory of the frequency comb output from a femtosecond fiber laser. *IEEE Journal of Quantum Electronics*, 41(11) :1388–1402, 2005.

[25] Jens Rauschenberger, Tara M Fortier, David J Jones, Jun Ye, and Steven T Cundiff. Control of the frequency comb from a mode-locked erbium-doped fiber laser. *Optics Express*, 10(24) :1404–1410, 2002.

[26] DK Armani, TJ Kippenberg, SM Spillane, and KJ Vahala. Ultra-high-q toroid microcavity on a chip. *Nature*, 421(6926) :925, 2003.

[27] Alessia Pasquazi, Marco Peccianti, Luca Razzari, David J Moss, Stéphane Coen, Miro Erkintalo, Yanne K Chembo, Tobias Hansson, Stefan Wabnitz, Pascal DelaHaye, et al. Micro-combs : a novel generation of optical sources. *Physics Reports*, 729 :1–81, 2018.

[28] Hiroshi Murata, Akhiro Morimoto, Tetsuro Kobayashi, and Sadahiko Yamamoto. Optical pulse generation by electrooptic-modulation method and its application to integrated ultrashort pulse generators. *IEEE Journal of Selected Topics in Quantum Electronics*, 6(6) :1325–1331, 2000.

[29] Adam J Fleisher, David A Long, Zachary D Reed, Joseph T Hodges, and David F Plusquellic. Coherent cavity-enhanced dual-comb spectroscopy. *Optics express*, 24(10) :10424–10434, 2016.

[30] Roy J Kennedy. A refinement of the michelson-morley experiment. *Proceedings of the National Academy of Sciences*, 12(11) :621–629, 1926.

[31] J.C. Diels, W. Rudolph, P.F. Liao, and P. Kelley. *Ultrashort Laser Pulse Phenomena*. Optics and photonics. Elsevier Science, 2006.

[32] Chris Chatfield. *The analysis of time series : an introduction*. CRC press, 2016.

[33] TJ Balle and WH Flygare. Fabry–perot cavity pulsed fourier transform microwave spectrometer with a pulsed nozzle particle source. *Review of Scientific Instruments*, 52(1) :33–45, 1981.

[34] M Vaughan. *The Fabry-Perot interferometer : history, theory, practice and applications*. Routledge, 2017.

[35] David Hunger, Tilo Steinmetz, Yves Colombe, Christian Deutsch, Theodor W Hänsch, and Jakob Reichel. A fiber fabry–perot cavity with high finesse. *New Journal of Physics*, 12(6) :065038, 2010.

[36] Ian Coddington, Nathan Newbury, and William Swann. Dual-comb spectroscopy. *Optica*, 3(4) :414–426, 2016.

[37] David A Naylor and Margaret K Tahic. Apodizing functions for fourier transform spectroscopy. *JOSA A*, 24(11) :3644–3648, 2007.

[38] Chi Hyung Seo and Jesse T Yen. Sidelobe suppression in ultrasound imaging using dual apodization with cross-correlation. *IEEE transactions on ultrasonics, ferroelectrics, and frequency control*, 55(10) :2198–2210, 2008.

[39] D Haertle, M Jazbinšek, G Montemezzani, and P Günter. Nonlinear optical coefficients and phase-matching conditions in sn 2 p 2 s 6. *Optics express*, 13(10) :3765–3776, 2005.

[40] Robert W Boyd. *Nonlinear optics*. Elsevier, 2003.

[41] Geoffrey New. *Introduction to nonlinear optics*. Cambridge University Press, 2011.

[42] *Basic Nonlinear Optics*. www.physics.ttk.pte.hu, 2013.

[43] Sergey A Ponomarenko. Fundamentals of nonlinear optics". *Dalhousie university*, page 77, 2015.

[44] Francesca Parmigiani, Christophe Finot, Kazunori Mukasa, Morten Ibsen, Michael AF Roelens, Periklis Petropoulos, and David J Richardson. Ultra-flat spm-broadened spectra in a highly nonlinear fiber using parabolic pulses formed in a fiber bragg grating. *Optics Express*, 14(17) :7617–7622, 2006.

[45] M. N. Islam, L. F. Mollenauer, R. H. Stolen, J. R. Simpson, and H. T. Shang. Cross-phase modulation in optical fibers. *Opt. Lett.*, 12(8) :625–627, Aug 1987.

[46] Raymond Y Chiao, E Garmire, and Charles H Townes. Self-trapping of optical beams. *Physical Review Letters*, 13(15) :479, 1964.

[47] Daniele Faccio, Paolo Di Trapani, Stefano Minardi, Alberto Bramati, Francesca Bragheri, Carlo Liberale, Vittorio Degiorgio, Audrius Dubietis, and Aidas Matijosius. Far-field spectral characterization of conical emission and filamentation in kerr media. *JOSA B*, 22(4) :862–869, 2005.

[48] Thomas Brabec, Ch Spielmann, PF Curley, and Ferenc Krausz. Kerr lens mode locking. *Optics letters*, 17(18) :1292–1294, 1992.

[49] Galina Khitrova, Paul R Berman, and Murray Sargent. Theory of pump–probe spectroscopy. *JOSA B*, 5(1) :160–170, 1988.

[50] AS Woutersen, U Emmerichs, and HJ Bakker. Femtosecond mid-ir pump-probe spectroscopy of liquid water : Evidence for a two-component structure. *Science*, 278(5338) :658–660, 1997.

[51] Patanjali Kambhampati, Dong Hee Son, Tak W Kee, and Paul F Barbara. Solvent effects on vibrational coherence and ultrafast reaction dynamics in the multicolor pump- probe spectroscopy of intervalence electron transfer. *The Journal of Physical Chemistry A*, 104(46) :10637–10644, 2000.

[52] Felix Frank, C Arrell, T Witting, WA Okell, J McKenna, JS Robinson, CA Haworth, D Austin, H Teng, IA Walmsley, et al. Invited review article : technology for attosecond science. *Review of Scientific Instruments*, 83(7) :52, 2012.

[53] Martin C Fischer, Jesse W Wilson, Francisco E Robles, and Warren S Warren. Invited review article : pump-probe microscopy. *Review of Scientific Instruments*, 87(3) :031101, 2016.

[54] Akifumi Asahara and Kaoru Minoshima. Development of ultrafast time-resolved dual-comb spectroscopy. *APL Photonics*, 2(4) :041301, 2017.

[55] Christoph Affolderbach, Fabien Droz, and Gaetano Mileti. Experimental demonstration of a compact and high-performance laser-pumped rubidium gas cell atomic frequency standard. *IEEE Transactions on Instrumentation and Measurement*, 55(2) :429–435, 2006.

[56] L Essen, EG Hope, and D Sutcliffe. Hyperfine splitting of rubidium-87. *Nature*, 189(4761) :298, 1961.

[57] Daniel A Steck. Rubidium 87 d line data, 2001.

[58] Jean-Daniel Deschênes, Philippe Giaccari, and Jérôme Genest. Optical referencing technique with cw lasers as intermediate oscillators for continuous full delay range frequency comb interferometry. *Optics Express*, 18(22) :23358–23370, 2010.

[59] Simon Potvin and Jérôme Genest. Dual-comb spectroscopy using frequency-doubled combs around 775 nm. *Optics express*, 21(25) :30707–30715, 2013.

[60] Jane Hodgkinson, Dackson Masiyano, and Ralph P Tatam. Using integrating spheres as absorption cells : path-length distribution and application of beer's law. *Applied optics*, 48(30) :5748–5758, 2009.

[61] J Christopher Dainty. *Laser speckle and related phenomena*, volume 9. Springer science & business Media, 2013.

[62] Iouli E Gordon, Laurence S Rothman, Christian Hill, Roman V Kochanov, Y Tan, Peter F Bernath, Manfred Birk, V Boudon, Alain Campargue, KV Chance, et al. The hitran2016 molecular spectroscopic database. *Journal of Quantitative Spectroscopy and Radiative Transfer*, 203 :3–69, 2017.

[63] Simon Potvin and Jérôme Genest. Reducing the effect of integrating sphere speckle when characterizing the instrument line shape of a fourier-transform hyperspectral imager. *Applied optics*, 48(30) :5849–5852, 2009.

[64] Murat Durak, Farhad Samadov, and A KAMURAN TÜRKOĞLU. Spatial non-uniformity measurements of large area silicon photodiodes. *Turkish Journal of Physics*, 26(5) :375–380, 2002.

[65] Nathan R Newbury, BR Washburn, Kristan L Corwin, and RS Windeler. Noise amplification during supercontinuum generation in microstructure fiber. *Optics letters*, 28(11) :944–946, 2003.

[66] Brian R Washburn and Nathan R Newbury. Phase, timing, and amplitude noise on supercontinua generated in microstructure fiber. *Optics Express*, 12(10) :2166–2175, 2004.

[67] M. Schonleber. A simple derivation of the kramers-kronig relations from the perspective of system theory.

[68] John Bechhoefer. Kramers–kronig, bode, and the meaning of zero. *American Journal of Physics*, 79(10) :1053–1059, 2011.

[69] Xin Gai, Duk-Yong Choi, Steve Madden, and Barry Luther-Davies. Materials and structures for nonlinear photonics. In *All-Optical Signal Processing*, pages 1–33. Springer, 2015.

[70] Th Udem, Ronald Holzwarth, and Theodor W Hänsch. Optical frequency metrology. *Nature*, 416(6877) :233, 2002.

[71] David J Jones, Scott A Diddams, Jinendra K Ranka, Andrew Stentz, Robert S Windeler, John L Hall, and Steven T Cundiff. Carrier-envelope phase control of femtosecond mode-locked lasers and direct optical frequency synthesis. *Science*, 288(5466) :635–639, 2000.

[72] Albert Schliesser, Markus Brehm, Fritz Keilmann, and Daniel W van der Weide. Frequency-comb infrared spectrometer for rapid, remote chemical sensing. *Optics Express*, 13(22) :9029–9038, 2005.

[73] Christophe Daussy, Olivier Lopez, Anne Amy-Klein, A Goncharov, Mickael Guinet, Christian Chardonnet, François Narbonneau, Michel Lours, Damien Chambon, Sébastien Bize, et al. Long-distance frequency dissemination with a resolution of 10- 17. *Physical review letters*, 94(20) :203904, 2005.

[74] VE Zakharov and LA Ostrovsky. Modulation instability : the beginning. *Physica D : Nonlinear Phenomena*, 238(5) :540–548, 2009.

[75] Charles Henry. Theory of the linewidth of semiconductor lasers. *IEEE Journal of Quantum Electronics*, 18(2) :259–264, 1982.

[76] Akifumi Asahara, Akiko Nishiyama, Satoru Yoshida, Ken-ichi Kondo, Yoshiaki Nakajima, and Kaoru Minoshima. Dual-comb spectroscopy for rapid characterization of complex optical properties of solids. *Optics letters*, 41(21) :4971–4974, 2016.

[77] A Russell Schaefer, Edward F Zalewski, and Jon Geist. Silicon detector nonlinearity and related effects. *Applied Optics*, 22(8) :1232–1236, 1983.

[78] DB Chase. Nonlinear detector response in ft-ir. *Applied spectroscopy*, 38(4) :491–494, 1984.

[79] Xiaoliang Wang, Qiang Fu, Jinfang Sheng, Xin Yang, Jianzhong Jia, and Wei Du. Construction of a universal quantitative model for ibuprofen sustained-release capsules from different manufacturers using near-infrared diffuse reflection spectroscopy. *Vibrational Spectroscopy*, 53(2) :214–217, 2010.

[80] Yuta Miyamae, Yumika Yamakawa, and Yukihiro Ozaki. Evaluation of physical properties of human hair by diffuse reflectance near-infrared spectroscopy. *Applied spectroscopy*, 61(2) :212–217, 2007.

[81] Marina Zoccola, Raffaella Mossotti, Riccardo Innocenti, Dora I Loria, Stefano Rosso, and Roberto Zanetti. Near infrared spectroscopy as a tool for the determination of eumelanin in human hair. *Pigment cell research*, 17(4) :379–385, 2004.

[82] David F Eaton. Nonlinear optical materials. *Science*, 253(5017) :281–287, 1991.